Lee-Wave Resonances over Double Bell-Shaped Obstacles

VANDA GRUBIŠIĆ*

Desert Research Institute, Reno, Nevada

IVANA STIPERSKI

Croatian Meteorological and Hydrological Service, Zagreb, Croatia

(Manuscript received 11 July 2008, in final form 2 October 2008)

ABSTRACT

Lee-wave resonance over double bell-shaped obstacles is investigated through a series of idealized high-resolution numerical simulations with the nonhydrostatic Coupled Ocean–Atmosphere Mesoscale Prediction System (COAMPS) model using a free-slip lower boundary condition. The profiles of wind speed and stability as well as terrain derive from observations of lee-wave events over the Sierra Nevada and Inyo Mountains from the recently completed Terrain-Induced Rotor Experiment (T-REX).

Numerical experiments show that double bell-shaped obstacles promote trapped lee waves that are in general shorter than those excited by an isolated ridge. While the permissible trapped lee-wave modes are determined by the upstream atmospheric structure, primarily vertical wind shear, the selected lee-wave wavelengths for two obstacles that are close or equal in height are dictated by the discrete terrain spectrum and correspond to higher harmonics of the primary orographic wavelength, which is equal to the ridge separation distance. The exception is the smallest ridge separation distance examined, one that corresponds to the Owens Valley width and is closest to the wavelength determined by the given upstream atmospheric structure, for which the primary lee-wave and orographic wavelengths were found to nearly coincide.

The influence two mountains exert on the overall lee-wave field is found to persist at very large ridge separation distances. For the nonlinear nonhydrostatic waves examined, the ridge separation distance is found to exert a much stronger control over the lee-wave wavelengths than the mountain half-width. Positive and negative interferences of lee waves, which can be detected through their imprint on wave drag and wave amplitudes, were found to produce appreciable differences in the flow structure mainly over the downstream peak, with negative interference characterized by a highly symmetric flow pattern leading to a low drag state.

1. Introduction

Stably stratified airflow over an isolated bell-shaped obstacle and attendant generation of terrain-induced perturbations has received considerable attention over the years in theoretical and numerical as well as experimental studies (Queney et al. 1960; Smith 1979; Baines 1995). In contrast, the flow over a double barrier, or more generally multiple-barrier problem, has been treated only to a limited extent (e.g., Grisogono et al. 1993; Vosper 1996; Mayr and Gohm 2000; Lee et al. 2005).

A nearly ideal two-dimensional (2D) double-barrier system, known for its generation of large-amplitude trapped lee waves and rotors, is the Sierra Nevada–White–Inyo Mountains in eastern California (Fig. 1). Owens Valley, which lies in between these two mountain ranges, has been the site of several field investigations of mountain waves and rotors, from the Sierra Wave Project (SWP) in the 1950s (Grubišić and Lewis 2004) to the Terrain-Induced Rotor Experiment (T-REX) in 2006 (Grubišić et al. 2008). It was noted already in SWP that trapped lee waves of longer wavelengths, in particular wavelengths that were close to the ridge separation distance, were more likely to achieve large amplitudes (Holmboe and Klieforth 1957), suggesting a form of resonant response of the flow to the double-ridge forcing. Together with its pilot Sierra Rotors Project (SRP) in

* Current affiliation: Department of Meteorology and Geophysics, University of Vienna, Vienna, Austria.

Corresponding author address: Prof. Vanda Grubišić, Department of Meteorology and Geophysics, University of Vienna, Althanstrasse 14, A-1090 Vienna, Austria.
E-mail: vanda.grubisic@univie.ac.at

DOI: 10.1175/2008JAS2885.1

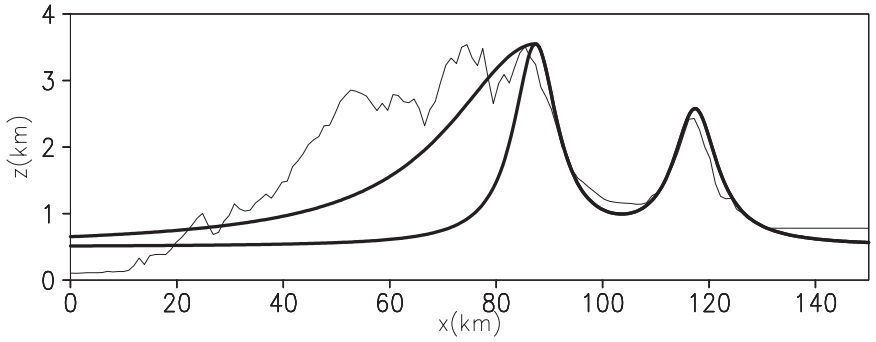

FIG. 1. SW–NE cross section of the Sierra Nevada–Inyo Mountains terrain (thin solid) through Independence, CA, at 36.78°N at the center of Owens Valley. Superimposed are idealized symmetric ($a = b = 5$ km) and asymmetric ($a = 5$ km; $b = 20$ km) double bell-shaped mountain profiles (solid bold) used in the simulations.

2004, T-REX has once again drawn attention to the phenomenon of trapped lee waves and rotors over Owens Valley. Preliminary T-REX observational evidence indicates that the prevailing wave response at lower-tropospheric levels has a form of partially trapped lee waves with an integral number of wave crests spanning the width of the valley. T-REX observations also lend further credence to the SWP findings that waves with longer horizontal wavelengths achieve larger amplitudes (Doyle et al. 2009).

A familiar atmospheric resonance phenomenon related to nonhydrostatic mountain waves belongs to trapped lee waves downwind of a single obstacle, in which the upward and downward propagating internal gravity waves interfere positively to produce a lee-wave pattern characterized by vertical phase lines and horizontal propagation of wave energy downwind of the generating terrain (Scorer 1949; Wurtele et al. 1987, 1996). The downward propagating waves result from partial or total reflection of terrain-generated internal gravity waves due to inhomogeneities in the atmospheric vertical structure, such as increases in wind speed and/or drops in stability that produce significant changes in wave propagation characteristics (Scorer 1949; Durran 1986). The horizontal wavelength of a trapped lee wave represents a resonant mode that is supported by the given atmospheric profiles of wind and stability and forced by the underlying terrain. In the small-amplitude approximation of the governing equations, this resonance is linear in the sense that the wavelength (or frequency) of the resonant oscillation is independent of its amplitude (Queney et al. 1960; Smith 1976).

In the context of the double-barrier problem, Vosper (1996) shows that, for linear trapped lee waves in the presence of upstream wind shear, the normalized gravity wave drag as a function of valley width exhibits oscillatory character even for very wide valleys. He attributes this oscillation to the constructive and destructive interferences of the partially trapped part of the wave spectrum excited by the two mountains. The maxima are evidence of constructive interference occurring for valley widths that are an integral multiple of horizontal wavelength of the partially trapped wave. For a rotational case, Grisogono et al. (1993) also note an oscillatory behavior of wave drag as a function of mountain separation, which they attribute to the constructive and destructive interference of the excited small-amplitude inertia–gravity waves. Since linear models were employed in both of these studies, neither of them provides any insight into a possible role of nonlinear wave interactions in the double-barrier wave resonance phenomenon.

A limited insight into the nonlinear regime of flow is provided by the towing tank experiments of Gyüre and Jánosi (2003), with which they scrutinize the classic concept of linear lee-wave interference over a double mountain barrier in nonhydrostatic flows with uniform stability and flow speed. While they find the wave response downwind of the second obstacle to be stronger than that over the valley, there is no evidence in their experiments of positive interference occurring for the second mountain placed at a distance equal to an integral multiple of lee-wave wavelengths downwind of the first. Instead, average wavelengths and amplitudes for two mountains were found to be systematically lower than those measured downwind of a single mountain. That, in addition to the observed fast decay of waves downstream of the second obstacle, suggests the presence of significant nonlinear effects in these experiments.

All of the above studies provide only limited guidance regarding possible lee-wave resonances in the Owens Valley environment, where the terrain slopes are steep, generated waves are of finite amplitude, and a typical upstream sounding is characterized by strong positive

vertical wind shear and pronounced temperature inversions at or above ridge height. The above characteristics of the upstream soundings were present also in the strongest lee-wave event of the SRP campaign, examined by Grubišić and Billings (2007). Using real-data simulations, they showed that significant sensitivity of trapped lee-wave response to the downstream orography exists during certain stages of the examined event. The sensitivity experiment in which the White–Inyo Mountains were removed produced horizontal wavelengths shorter by as much as 15 km (~40%) compared to those in the baseline run (cf. Fig. 20 in Grubišić and Billings 2007)—the effect opposite to that observed by Gyüre and Jánosi (2003) in their laboratory experiments. In this study, we investigate in more detail these sensitivities with a series of idealized high-resolution 2D numerical simulations with double bell-shaped orography, focusing in particular on potential lee-wave resonances in the nonlinear and nonhydrostatic flow regime in the absence of rotation.

The paper is organized as follows: The numerical model and experimental setup are presented in section 2, and the numerical experiments and diagnostics used are explained in section 3. Section 4 delivers the results, which are further discussed in section 5. Section 6 concludes the paper.

2. Numerical model and experimental setup

The numerical simulations were carried out using the atmospheric component of the Naval Research Laboratory (NRL) Coupled Ocean–Atmosphere Mesoscale Prediction System (COAMPS; Hodur 1997). This nonhydrostatic, fully compressible model was run in the 2D mode, simulations otherwise being free-slip, irrotational, and dry. The model runs were initialized by an impulsive start from rest using an idealized horizontally homogenous sounding. Of the physical parameterizations, only the subgrid-scale mixing based on the prognostic equation for turbulent kinetic energy (Mellor and Yamada 1982) was used.

Following Grisogono et al. (1993), the basic terrain profile is defined as a superposition of two single Witch of Agnesi obstacles:

$$h(x) = \frac{H_1 a^2}{a^2 + (x + V/2)^2} + \frac{H_2 a^2}{a^2 + (x - V/2)^2}, \qquad (1)$$

where H_1 and H_2 are the heights of the first (upstream) and second (downstream) bell-shaped obstacle, a is the mountain half-width, and V is the ridge separation distance (i.e., valley width). With the terrain parameters set to $H_1 = 3000$ m, $H_2 = 2000$ m, $a = 5$ km, and $V = 30$ km, the above terrain profile captures the essential features of the Owens Valley topography, in particular steep valley-side gradients of the Sierra Nevada and the Inyo range (Fig. 1). In the majority of experiments in this study we have used the above symmetric mountain profiles. The Sierra Nevada, however, has a highly asymmetric profile with the gentle upwind and steep lee-side slope. To investigate the effect of the mountain asymmetry, in a limited number of experiments the upstream mountain was replaced by

$$h_1(x) = \begin{cases} \dfrac{H_1 b^2}{b^2 + (x + V/2)^2} & x < -V/2 \\ \dfrac{H_1 a^2}{a^2 + (x + V/2)^2} & x \geq -V/2 \end{cases}, \qquad (2)$$

where b is the windward and a the leeward mountain half-width. In these experiments, b is varied between 5 and 20 km (cf. Fig. 1). While in the majority of experiments in this study $a = 5$ km, in a limited number of experiments wider symmetric obstacles have been used as well ($a = b = 10$–15 km).

The numerical domain is centered on the valley axis between the two peaks. The horizontal extent of the domain in the x direction (wind parallel) was varied depending on the ridge separation in such a way that the upstream and downstream lateral boundaries were always placed at a distance of approximately 105 km from, respectively, the first and the second mountain crest. The horizontal grid spacing is 400 m. The number of horizontal grid points in the x direction ranges from 601 to 1001 depending on a particular experiment. In the vertical, 111 nonuniformly spaced sigma levels were used. The vertical grid spacing decreases from 100 m at the ground to 55 m in the inversion layer (located at 5150 m) and then increases continuously to 500 m toward the top of the model domain at 26 km. In the uppermost 16 km of the domain, Raleigh damping is applied, where all fields are relaxed to their mean state values. As lateral boundary conditions, radiation and extrapolation condition is used in the x direction, whereas periodic boundary condition is specified in the y direction. All simulations employ a fourth-order advection scheme (Reinecke and Durran 2009). The time step is equal to 1 s, with four small time steps needed to properly handle sound waves. All simulations were initialized with an impulsive start from rest. The majority of experiments were run for 17 h ($U_H t/a = 222$, where U_H is the wind speed at crest height and t is the run time). By that time, a quasi–steady state was reached and maintained over several hours (over $U_H t/a \approx 40$) in the majority of experiments. Exceptions are experiments with a single mountain and low height of the secondary obstacle, as well as experiments with weak shear, which require longer time to reach a quasi–steady state and were run up to $t = 25$ h.

The above model setup was employed in the set of verification runs in which the obtained value of mountain-wave drag, due to small-amplitude hydrostatic waves over twin peaks in the absence of rotation, was within 1% of the analytical value given by Grisogono et al. (1993).

The baseline sounding is a simplified version of the atmospheric sounding obtained upstream of the Sierra Nevada at 0000 UTC 26 March 2004 during SRP intensive observation period (IOP) 8 (Fig. 2). The selected sounding falls at the beginning of a time period during which real-data simulations of Grubišić and Billings (2007) show the largest sensitivity to the downstream orography. The vertical profile of the barrier-normal component of wind in this sounding is characterized by a four-layer structure consisting of a nearly stagnant layer near the ground, a deep layer of positive shear in the midtroposphere extending to a ''nose'' of a pronounced jet, and a decrease of wind speed in the stratosphere. Such vertical atmospheric structure is commonly observed in many strong lee-wave events upstream of the Sierra Nevada. As illustrated in Fig. 2, the selected sounding shares many characteristics with the 1400 UTC 25 March 2008 sounding from T-REX IOP 6, which is one of the strongest T-REX lee-wave events. In the simplified sounding, the wind speed increases linearly from zero at the ground to the maximum at approximately 7.5 km, above which a 4-km-thick constant-wind-speed layer was placed. To preserve the midtropospheric shear ($\sim$6.1 m s^{-1} km^{-1}), the jet maximum was increased by approximately 20% above the observed values to 45.5 m s^{-1}. In the stratosphere, the wind speed decreases linearly with height, reaching zero at the top of the model domain. The potential temperature profile is characterized by a three-layer structure that was also represented by a piecewise linear function. The two tropospheric layers of constant stability, where stability is defined by the Brunt–Väisälä frequency ($N^2 = g/\theta\ \partial\theta/\partial z$), are separated by a strong inversion (0.044 K m^{-1}) with a base at z_i = 5150 m. To achieve better resolution, the depth of the inversion in the idealized profile was increased to 110 m while the original gradient across it was retained. The Brunt–Väisälä frequencies in the layers below and above the inversion are N_L = 0.012 s^{-1} and N_U = 0.01 s^{-1}, respectively. The profile of the Scorer parameter[1] l is characterized by a strong decrease in the troposphere with a sharp peak at the inversion. Characteristics of this baseline sounding and its variations considered in this study are summarized in Table 1.

3. Numerical experiments and diagnostic parameters

As the main objective of this study is to examine sensitivities to the terrain shape of lee waves that are supported by the atmospheric profile described in the previous section, we have performed three sets of numerical experiments to determine the effects of mountain height, valley width, and mountain asymmetry on the flow field. Two additional sets of simulations were conducted to investigate the sensitivity of generated waves to certain elements of the upstream profile, specifically, the near-mountaintop inversion and strength of the vertical wind shear.

With the values of baseline sounding low-level stability (N_L) and wind speed at crest height (U_H) (cf. Table 1), the nondimensional mountain height of $H_1N_L/U_H \approx 2$ for H_1 = 3000 m puts our simulated 2D flows in the strongly nonlinear regime, in which upstream blocking and an upstream propagating columnar mode are expected (Pierrehumbert and Wyman 1985; Baines 1995). However, the nonlinearity of the simulated flows is actually weaker compared to what would be expected for the same nondimensional mountain height in the constant wind speed and stability case due to the effects of strong wind shear, as shown, among others, by Wang and Lin (2000). For constant stability N = 0.011 s^{-1} and range of shear S = 3–7 m s^{-1} km^{-1} (cf. Table 1), the Richardson number Ri = $N^2/(\partial U/\partial z)^2$ = 2.5–13. As noted by Wurtele et al. (1987) for a flow past an isolated ridge, the higher the Richardson number, the larger number of stationary modes exists at the shorter-wavelength end of the spectrum that could give rise to resonant lee waves. This helps to explain stronger nonsteadiness displayed in our simulations with weaker shear, and longer time needed in these experiments to settle to a specific stationary mode.

Several diagnostic parameters, determined from the model simulations, are used in the presentation and analysis of results in the following sections. Gravity wave drag [$D = \int p(dh/dx)dx$] was calculated using surface pressure and terrain data and was normalized by the linear analytic value for a double bell-shaped mountain from Grisogono et al. (1993) using N_L and U_H in their Eq. (8). Wave drag time series was used for determining the quasi-steady periods during which further data analysis was carried out. The steady-state value of drag was also used as a quantitative measure for detecting positive and negative wave interferences. In addition, we have used the wave amplitudes downwind of the

[1] Scorer parameter, l, is defined as $l^2 = N^2/U^2 - (\partial^2 U/\partial z^2)/U$. Given our piecewise-linear velocity profile, the second derivative is equal to zero everywhere except at the layer boundaries, where it is singular. Consequently, only the first term, N/U, was used in the computation of the Scorer parameter.

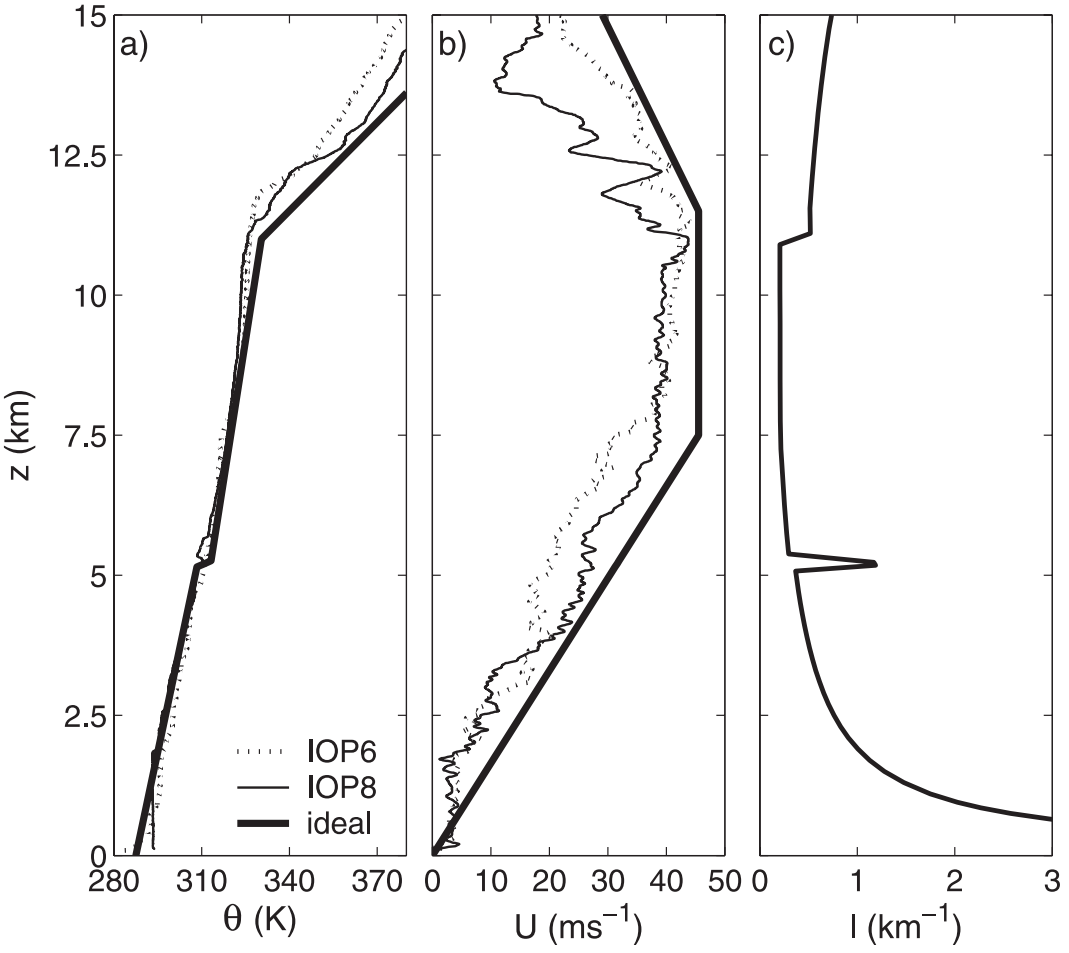

FIG. 2. Vertical profiles of (a) potential temperature, (b) cross-mountain wind speed, and (c) Scorer parameter from the idealized (bold solid line) and observed upstream soundings from SRP IOP 8 at 0000 UTC (thin solid line) and T-REX IOP 6 at 1400 UTC (thin dashed line).

upstream (A_1) and downstream mountain (A_2), which are defined as $A_i = [(W_{\max})_i - (W_{\min})_i]/2$, where $i = 1, 2$, and $W_{\max}$ and $W_{\min}$ are, respectively, the maximum and minimum of the vertical velocity within specific portions of the numerical domain (Fig. 3). In the vertical, these quantities were determined within a layer extending between 3 and 7 km. In the horizontal, the search for A_1 was limited to the area between the two peaks, and for A_2 over the area extending from the second peak to the downstream end of the domain.

The values of wave drag and amplitudes shown in the following sections represent time averages over the quasi-steady periods of our simulations, determined individually for each simulation. Drag was preferred over A_2 for detecting whether positive or negative interference has occurred, as it represents an integral measure of the flow field. The simulation results for twin peak experiments show a strong correlation ($r = 0.9$) between these two diagnostic parameters. Whereas in some simulations these quantities show very little variation over the averaging period, about 2% of the average value of drag, in a subset of simulations the variation was more pronounced, reaching up to 16% of the average value for drag. On average, the amplitude of

TABLE 1. Brunt–Väisälä frequencies in the layer below (N_L), at (N_i), and above (N_U) the inversion, vertical wind shear (S), and horizontal wind speed at mountain height (U_H) for the baseline run and experiments with no inversion and varied vertical wind shear.

	N_L (s^{-1})	N_i (s^{-1})	N_U (s^{-1})	S (m s^{-1} km^{-1})	U_H (m s^{-1})
Baseline	0.012	0.037	0.010	6.1	18.2
No inversion	0.011	0.011	0.011	6.1	18.2
$S = 3$	0.011	0.011	0.011	3	9
$S = 4$	0.011	0.011	0.011	4	12
$S = 5$	0.011	0.011	0.011	5	15
$S = 7$	0.011	0.011	0.011	7	21

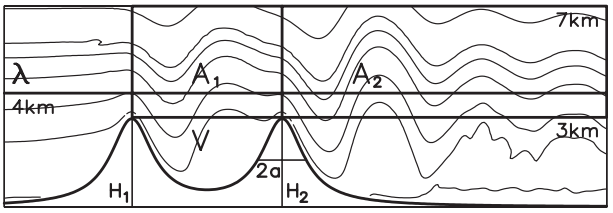

FIG. 3. Diagnostic parameters. Horizontal wavelength (λ), derived from potential temperature field at 4 km, and wave amplitudes A_1 and A_2, determined from extrema of vertical velocity field in the marked parts of the domain.

the drag variation was around 7%. As noted by Wurtele et al. (1999) this variation is the result of interference of propagating nonresonant modes that are, in addition to the resonant lee-wave mode, also excited by the impulsive start from rest.

Spectra of wave fields were determined from the potential temperature data at 4 km (Fig. 3) using fast Fourier transform (FFT). Orographic spectra were also determined for each of the mountain profiles from the Fourier transform of the mountain shape in Grisogono et al. (1993). Unless otherwise indicated, horizontal wavelengths λ refer to the primary peak of the lee wave and λ_{oro} to the peak of the orographic power spectra (Fig. 4).

In the presentation of results in the following section we make use of several nondimensional ratios. These include mountain height ratio H_n, defined as H_2/H_1, where $H_n = 0$ and ∞ signify a single mountain and $H_n = 1$ corresponds to two mountains of equal heights ("twin peaks"); amplitude ratio A_2/A_1; and nondimensional wavelength V/λ, defined as the ratio of the valley width to the horizontal wavelength.

4. Results

a. Terrain forcing

In this section we examine the sensitivities of flow solutions obtained with the baseline sounding to the terrain forcing. We start out by examining the sensitivity of the flow to the presence and height of a secondary obstacle and proceed to examine the sensitivities of the double bell-shaped mountain solutions to the ridge separation distance (valley width) and the asymmetry of the upwind mountain.

1) SECONDARY MOUNTAIN HEIGHT

In the experiments described in this section the secondary obstacle was placed either downstream (series 1) or upstream (series 2) of the primary obstacle and its height varied in the range 0–3000 m in 500-m increments. The height of the primary obstacle is fixed at 3000 m, and a and V are set at 5 and 30 km, respectively. This gives $H_n \in [0,1]$ for experiments in series 1 and $H_n \in [1,\infty)$ for series 2. Although the addition of a secondary mountain increases the effective height of both obstacles ($H_{\text{eff}} = 1.03H_1$ for $V = 30$ km and $H_1 = H_2$), this does not greatly increase the degree of flow nonlinearity (cf. Mayr and Gohm 2000).

Figure 5 shows the vertical cross sections of potential temperature and vertical velocity for different H_n from series 1 during the quasi-steady period of these simulations. The solutions in Fig. 5 are shown at $U_H t/a = 157$ ($t = 12$ h) except for $H_n = 0$, which is shown at $U_H t/a = 262$ ($t = 20$ h). For the atmospheric structure of the baseline sounding, a single bell-shaped obstacle produces partially trapped lee waves (Fig. 5a). The amplitude of these waves decays sharply downwind, resulting in a large-amplitude wave perturbation confined to the immediate lee of the obstacle. The wave phase lines are nearly vertical, indicating a high degree of vertical energy trapping, especially farther away from the obstacle, where flow gradually returns to the undisturbed state in the far lee. The wave amplitude maximizes near 5 km, at the altitude of the inversion. Trapped lee waves downwind of a single obstacle are expected for this atmospheric structure given the Scorer parameter profile that sharply decreases with height (Fig. 2). The horizontal wavelength of these trapped waves in the steady state is $\lambda_s = 24$ km, although at earlier times during the course of the simulation other horizontal wavelengths are dominant, primarily $\lambda = 30$ km. Given a continuous spectrum of a single bell-shaped obstacle (cf. Fig. 4), we take λ_s to represent an intrinsic wavelength for this given atmospheric vertical structure. As our simulations are free-slip, sharp downstream decay of the lee-wave amplitude cannot be attributed to surface friction. It is possible that this decay is a result of partial upward leakage of wave energy (cf. Fig. 5) or nonlinear interactions of excited wave modes as argued for internal gravity waves in the ocean downstream of a submerged ridge (Lozovatsky et al. 2003). However, turbulent dissipation occurring underneath the first few wave crests in the lee and wave absorption near the ground in a quiescent boundary layer are more likely causes of downstream decay in this case. We will come back to this point in section 5.

The introduction of the secondary obstacle downwind of the primary one alters the wave solution by increasing the degree of wave trapping and giving rise to the appearance of shorter horizontal wavelengths at levels below the inversion (Figs. 5b–d). The degree of wave trapping (i.e., downstream propagation of wave energy) and the wave amplitude in the immediate lee of the secondary obstacle, in general, increase as the height of the downstream mountain is increased, with a few irregularities

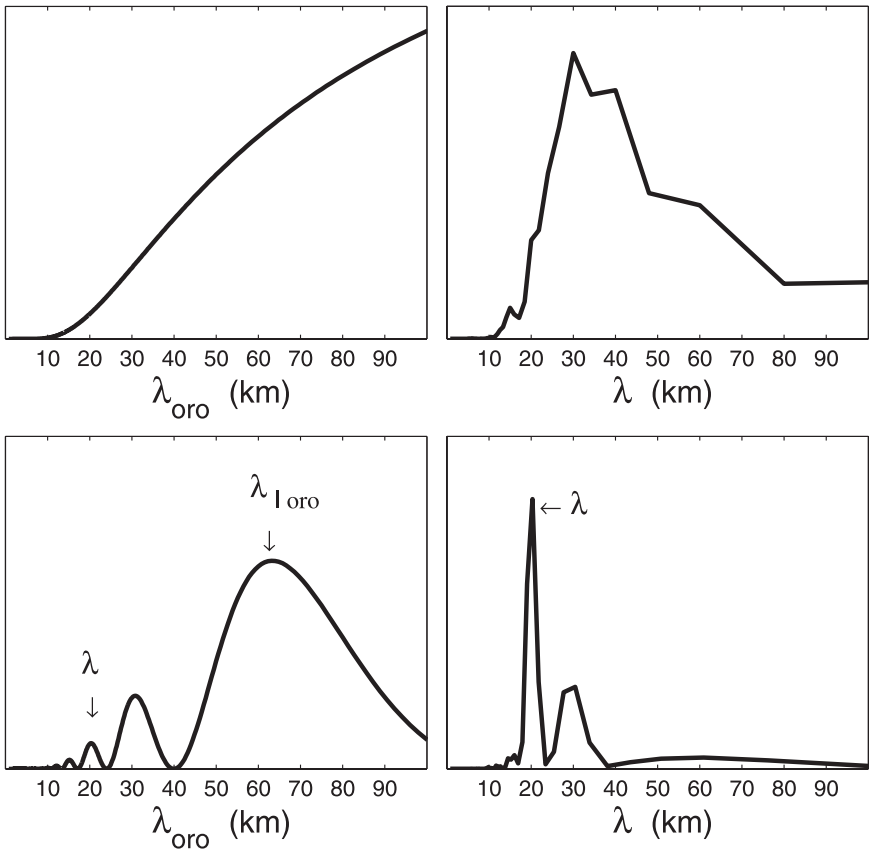

FIG. 4. (left) Orographic and (right) lee-wave power spectra as a function of wavelength for a (top) single mountain and (bottom) double mountain with $V = 60$ km. In the lower left panel, the primary orographic wavelength (λ_{oro}) and the wavelength closest to the primary lee wavelength ($\sim\lambda$) are marked. The y axes are not to scale.

such as for $H_n = 1/2$, for which a weaker wave solution and a shorter horizontal wavelength are obtained than for both slightly higher and lower downstream mountains. For $H_n = 2/3$, which is approximately equal to the height ratio of the Sierra Nevada and the Inyo Mountains, the solution displays the largest difference in the wave structure below and above the inversion. A similar strong effect on the overall wave solution is achieved by placing the secondary obstacle upwind of the primary one and by varying its height (series 2), but the exact details of solutions differ from those in series 1. Vertical cross sections of potential temperature and vertical velocity for a subset of experiments in series 2 are shown in Fig. 6.

The summary of these two series of experiments is shown in Fig. 7. For $H_n \leq 1$ the lee-wave wavelength stays close to or below λ_s with the exception of $H_n = 1$, for which $\lambda = 30$ km. For $H_n > 1$ a somewhat smaller range of primary wavelengths is obtained with a larger number of mountain height ratios generating the wavelengths longer than λ_s. Nevertheless, with the exception of very small secondary mountains, a similar effect on the wavelength is induced by the secondary obstacle of a given height, regardless of whether that obstacle is located on the upstream or downstream side of the primary one. The result is a range of nondimensional wavelengths V/λ between 1 and 1.5 for the examined range of $H_n \in [1/6, 6]$, with the maxima at $H_n = 1/6$ and 1/2 (Fig. 7b). The ratio of wave amplitudes downwind of the smaller to that downwind of the higher mountain (i.e., A_2/A_1 for $H_n \leq 1$ and its inverse A_1/A_2 for $H_n > 1$) follows the same general behavior in both cases, although that ratio is smaller for $H_n > 1$ since the lower upwind mountain lies partially or completely within the blocked layer on the upstream side of the higher downwind obstacle. These solutions clearly indicate that the influence of a lower upstream mountain range cannot be neglected even when the upstream mountain is considerably lower than the downstream one so that it lies entirely within the blocked layer on its upstream side.

In these experiments, the amplitude ratio A_2/A_1 exceeds unity for $H_n > 3/4$. This means that waves can achieve larger amplitudes in the lee of the downstream

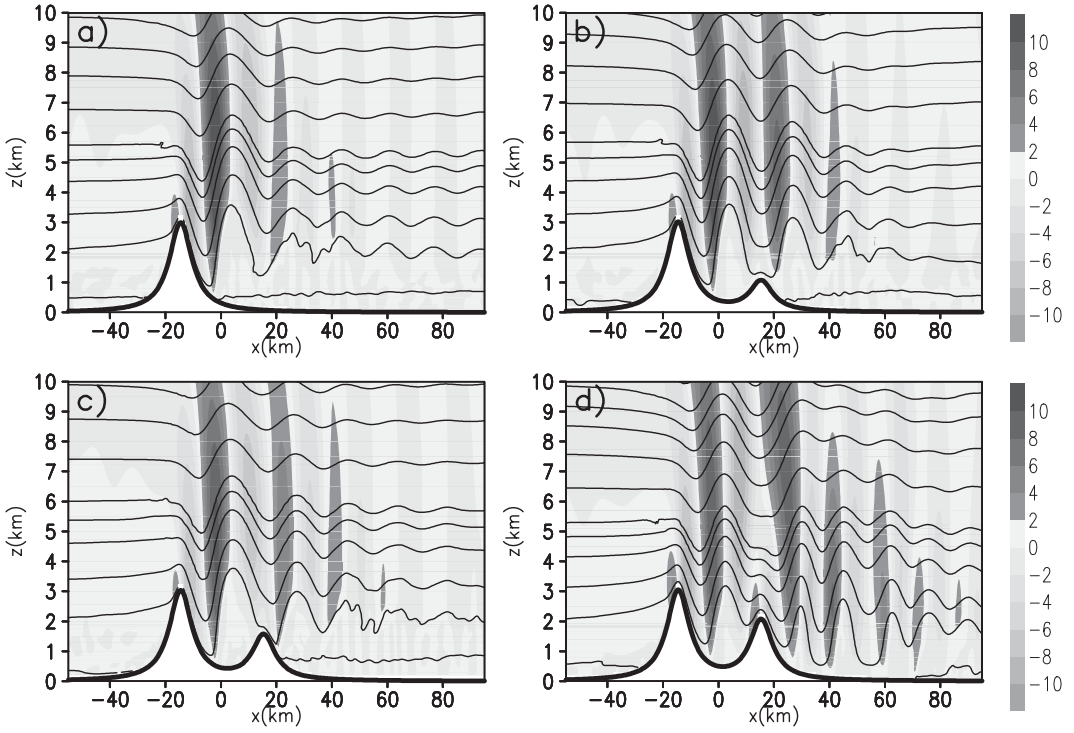

FIG. 5. Vertical cross sections of isentropes (solid lines; contouring interval 5 K) and vertical velocity (shaded; 2 m s^{-1} intervals) for $V = 30$ km and H_n equal to (a) 0 (and ∞), (b) 1/3, (c) 1/2, and (d) 2/3. Only the central portion of the domain is shown.

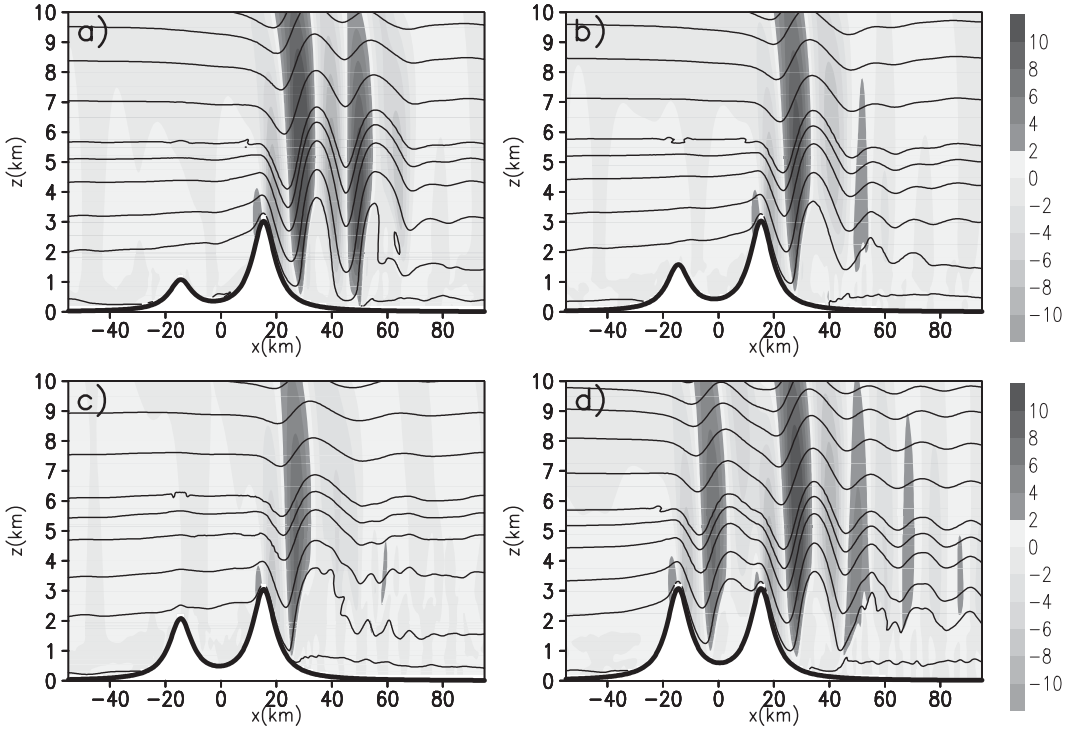

FIG. 6. As in Fig. 5 but for H_n equal to (a) 3, (b) 2, (c) 3/2, and (d) 1.

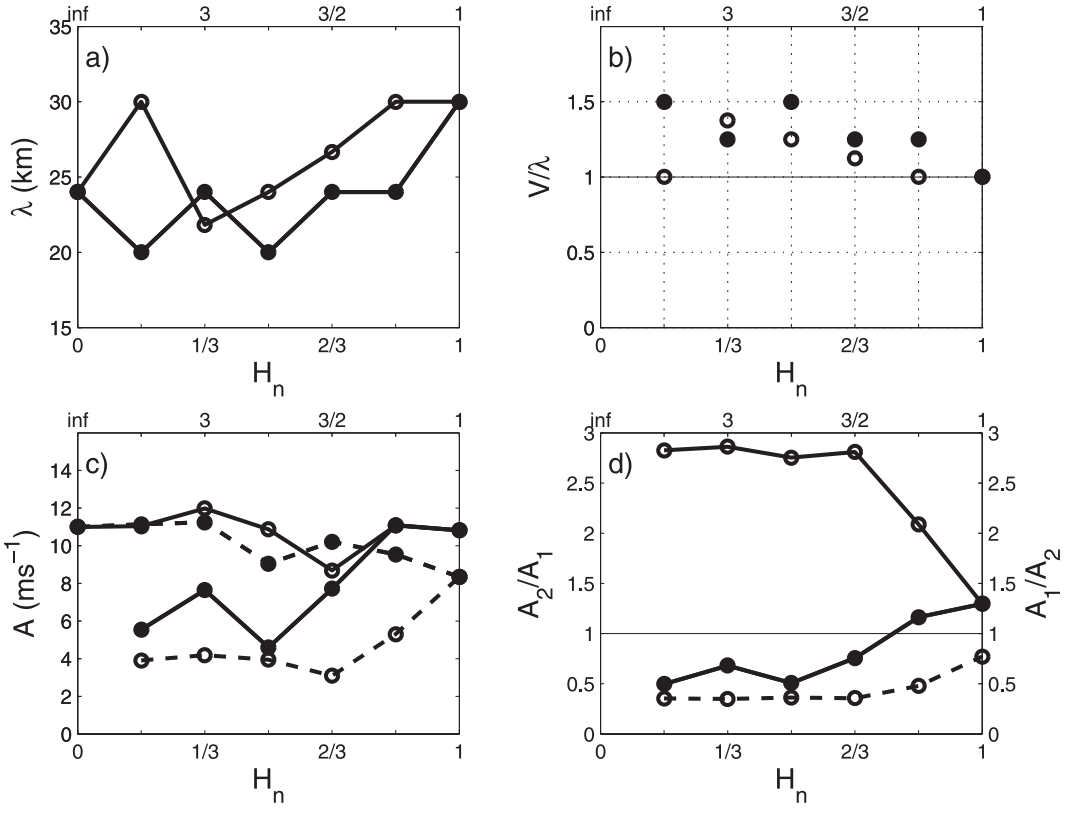

FIG. 7. Summary of mountain height sensitivity experiments: (a) horizontal wavelength (λ), (b) nondimensional wavelength (V/λ), (c) wave amplitudes A_1 (dashed line) and A_2 (solid line), and (d) amplitude ratio A_2/A_1 (solid) as functions of H_n. In (d) A_1/A_2 for experiments with $H_n > 1$ (dashed line) is also shown. Filled symbols denote experiments with a lower downstream mountain ($H_n < 1$; bottom x axis), and open symbols denote experiments with a lower upstream mountain ($H_n > 1$; top x axis). For definitions of diagnostic parameters, see section 3 and Fig. 3.

peak than over the valley even when the downstream mountain is lower than the upstream one. This also implies larger-amplitude wave perturbations in the lee of the downwind mountain than over the valley for twin peaks ($H_n = 1$), as noted previously by Tampieri and Hunt (1985), Vosper (1996), and Gyüre and Jánosi (2003).

2) VALLEY WIDTH

In this series of experiments the ridge separation distance V was varied between 30 and 180 km for $H_n = 1$. Vertical cross sections of potential temperature and vertical velocity for several V are illustrated in Fig. 8 with the summary of diagnostic parameters given in Fig. 9.

As the valley width is increased, the trapped wave solution in steady state (or quasi–steady state) adjusts to the new terrain shape (Fig. 8). The adjustment consists of an increase in the number of wave crests across the width of the valley with a preferential placement of a wave downdraft on the lee side of the downwind peak. As a result, we find that the nondimensional wavelengths cluster around integer values (Fig. 9b). Except for the ridge separation distance of $V = 30$ km, for which waves have $\lambda = 30$ km, as noted in the preceding section, all the other lee-wave wavelengths are shorter, ranging between 18.8 and 24 km (Fig. 9a). Thus, for the same atmospheric profile, twin peak orography promotes wavelengths that are equal or shorter than those excited by a single mountain. In addition, the excited waves have wavelengths that are an integer fraction of the ridge separation distance.

For all values of the ridge separation distance V examined in this series, A_1 is smaller than A_2, so that the amplitude ratio $A_2/A_1 > 1$, consistent with the findings described in the preceding section. Amplitudes in the lee of the downstream peak (A_2) exhibit variation with the valley width (Fig. 9c) that is reflected in wave drag as well (Fig. 9d). As A_1 displays less variation than A_2, the local maxima and minima of A_2/A_1 correlate well with the extrema of A_2. An example of the flow pattern for the minimum in A_2/A_1 at $V = 37$ km is shown in Fig. 8a. Even though V/λ is close to 2 for these waves, as is for a number of valley widths in the range from 35 to 50 km, the values of A_2 and D for this flow are markedly lower

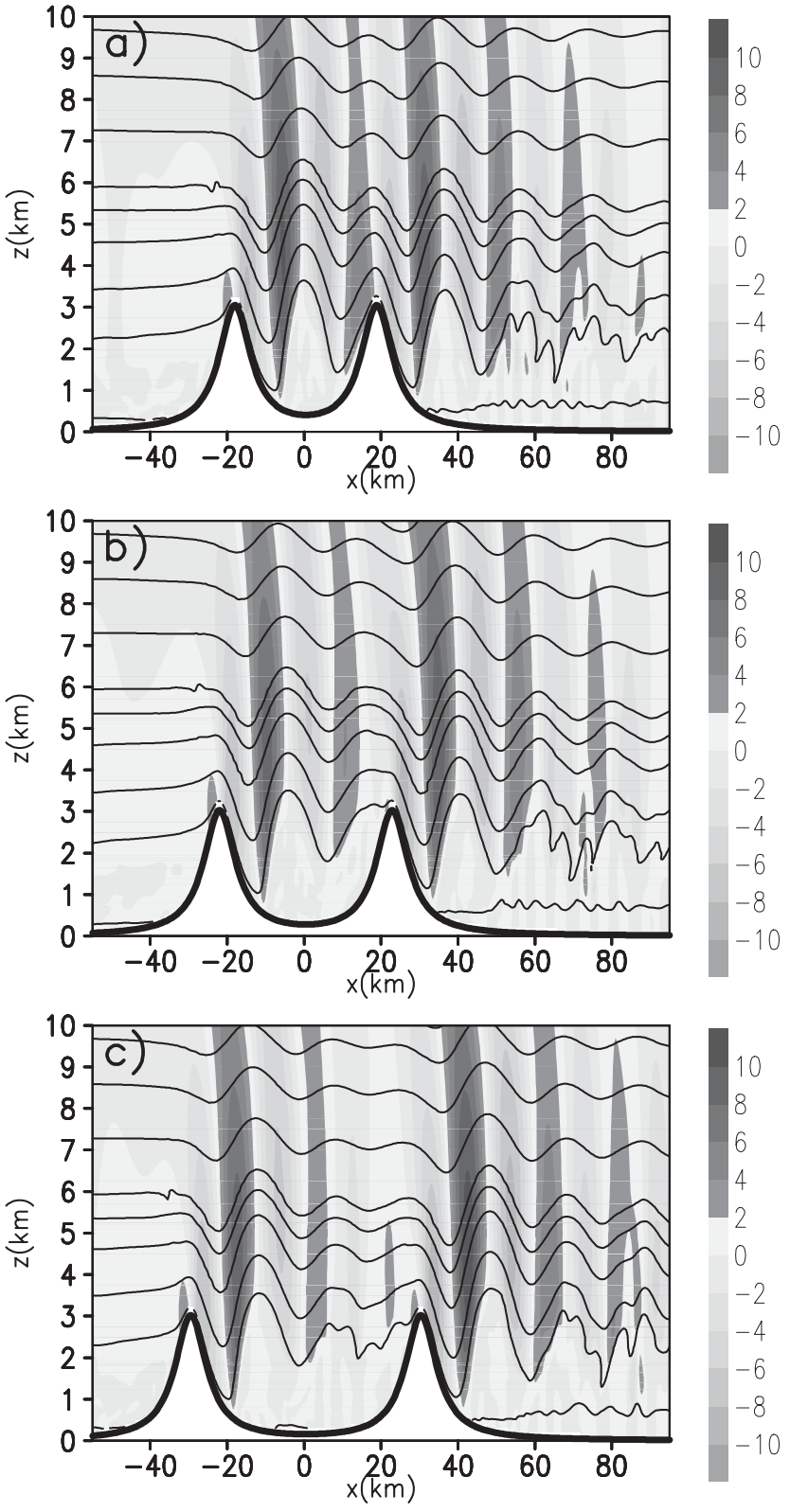

FIG. 8. As in Fig. 5 but for $H_n = 1$ and the ridge separation distance (V) equal to (a) 37, (b) 45, and (c) 60 km.

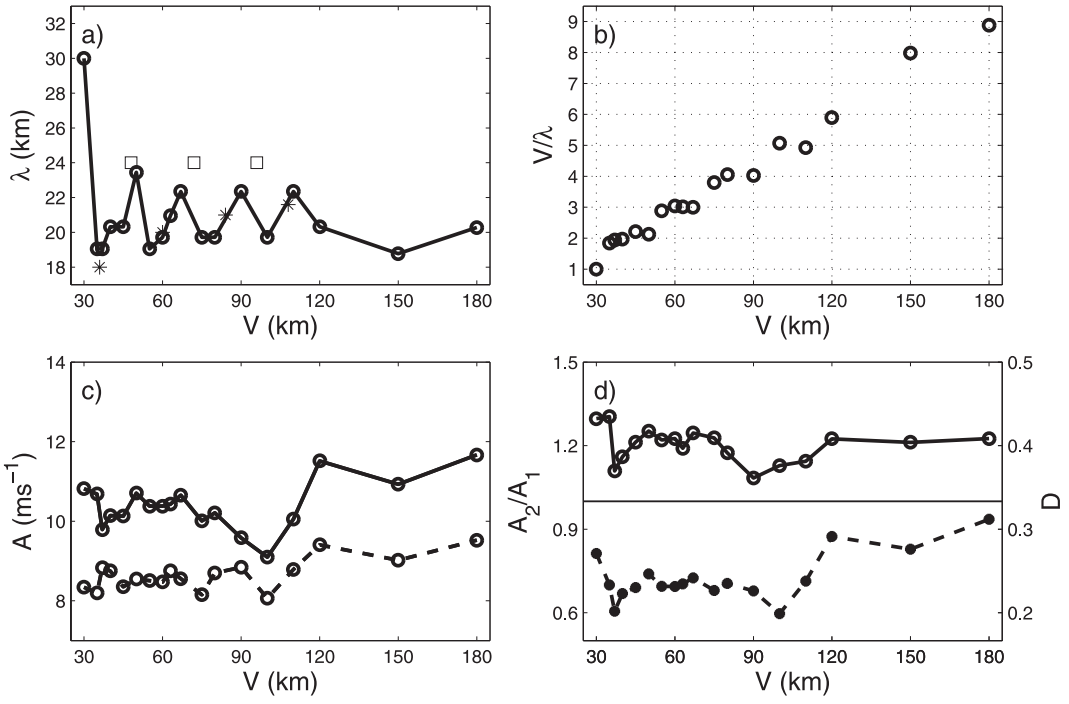

FIG. 9. As in Fig. 7 but for sensitivity experiments for the ridge separation distance with $H_n = 1$. In (a) predictions of a simple resonance model for constructive (squares) and destructive (stars) interferences are also marked. In (d) drag (dashed line; right y axis) is also shown.

than those for the neighboring valley widths. The lower value of drag in this and similar cases is a consequence of the flow symmetry over the downstream peak, which contributes very little or nothing to the total drag. As stated earlier, we take these drag (and amplitude) variations to be indicative of constructive and destructive interference of these nonlinear waves.

From the above results, it is clear that the two mountains at large separation distances continue to exert influence on each other and the overall flow field. This counters the expectation that placing the mountains sufficiently far apart would result in a localized wave disturbance downwind of each crest, as was the case in Grisogono et al. (1993) and Mayr and Gohm (2000). Even though these two studies dealt with hydrostatic waves, which are limited spatially to the area directly above the mountains, the expectation of diminishing influence appears reasonable in our case as well given the strongly decaying lee-wave solution downwind of a single mountain (cf. section 4a and Fig. 5). Yet, we do not see that in our experiments, even for the largest separation distance simulated ($V = 180$ km). Instead, $\lambda < \lambda_s$ and $A_1 < A_2$ for all V, although A_2 does seem to asymptotically approach A_s. The fact that A_1 remains smaller than A_2 could be due to the effects of flow stagnation within the valley. We will come back to the interaction of the two mountains in section 5.

3) UPSTREAM MOUNTAIN ASYMMETRY

Selected vertical cross sections from a series of experiments with the upwind half-width of the upstream mountain equal to 5, 10, 15, and 20 km are presented in Fig. 10 with the diagnostics shown in Fig. 11. In these experiments $H_n = 1$, $V = 30$ km, and $a = 5$ km. The results show that the primary lee-wave wavelength does not appear to be very sensitive to the change in b. Consequently, the nondimensional wavelength remains close to unity over the examined range of b values. The wave amplitudes are affected by mountain asymmetry but since the amplitude variations in the lee of the upstream and downstream mountain parallel each other, the resulting amplitude ratio A_2/A_1 is nearly constant over the examined range of b. The maxima in wave amplitude are obtained for $b = 10$ km, and the amplitudes decrease as the asymmetry of the upstream mountains increases.

These results suggest that the primary wavelength of trapped lee waves over the twin peaks is more strongly controlled by the ridge separation distance than the half-width of the mountains, contrary to what was suggested by Lee et al. (1987). The decrease of lee-side wave amplitudes with increasing upstream mountain asymmetry is also contrary to the expectation that a more strongly asymmetric upstream mountain would

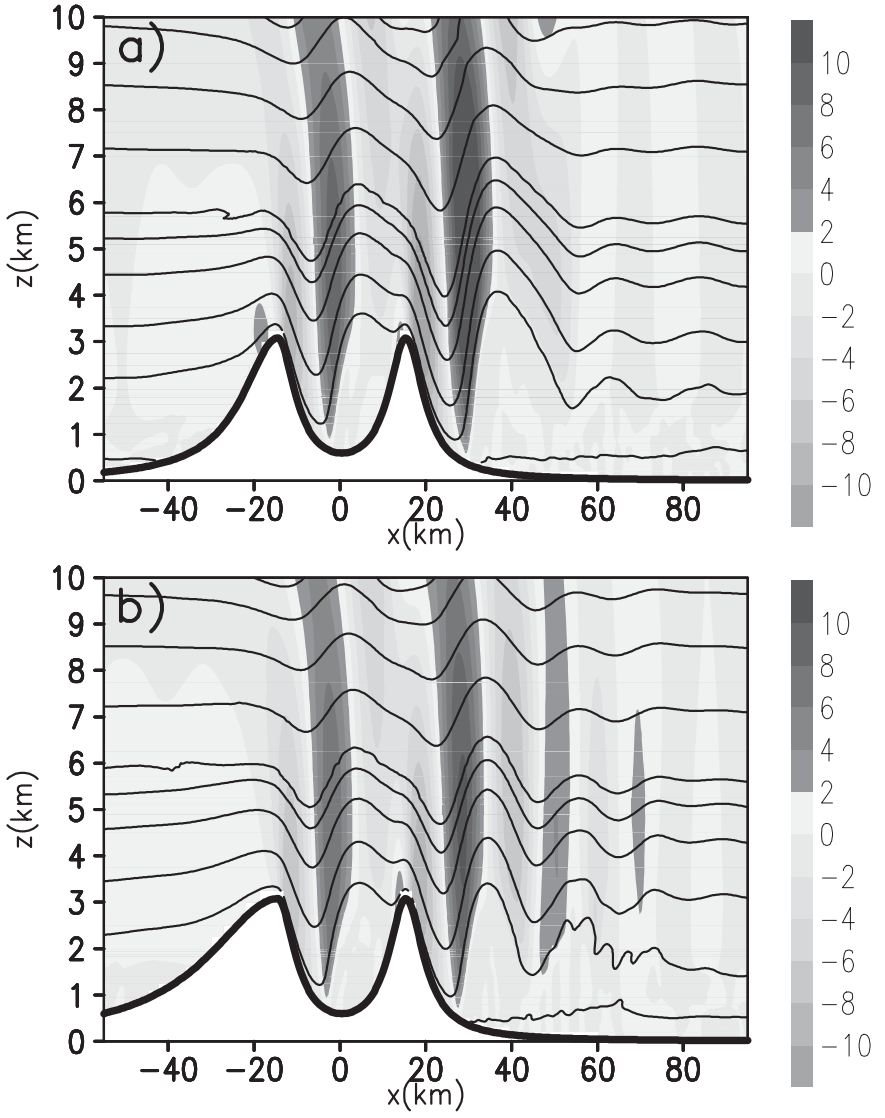

FIG. 10. As in Fig. 5 but for the upstream half-width b equal to (a) 10 and (b) 20 km; $H_n = 1$ and $V = 30$ km.

tend to promote stronger lee-side motions (Lilly and Klemp 1979). The same expectation also derives from single obstacle experiments of Miller and Durran (1991), who show that severe downslope windstorms develop more readily over asymmetric mountains, even in the absence of friction in their free-slip numerical experiments. Clearly, the existence of a valley in between twin peaks at small separation distances has a strong modulating effect, and it is conceivable that solutions at large separations distances would display somewhat different sensitivity to the upstream mountain asymmetry.

b. *Upstream atmospheric structure*

Given the known sensitivities of lee-wave solutions to the details of the upstream atmospheric structure (Holmboe and Klieforth 1957; Hertenstein and Kuettner 2003; Vosper 2004), here we examine separately the effects of the inversion from those of the vertical wind shear on lee waves over double bell-shaped mountains.

1) INVERSION

To isolate the effects of the inversion, we have replaced the three-layer stability structure of the baseline sounding with a constant tropospheric stability profile ($N = 0.011$ s^{-1}; cf. Table 1). With this altered stability profile we repeated series 1 experiments from section 4a(1) ($H_n \in [0,1]$, $a = b = 5$ km, $V = 30$ km). Results in Fig. 12 indicate that the inversion at this particular height above the upstream mountain peak has little effect on the wavelength. The inversion clearly

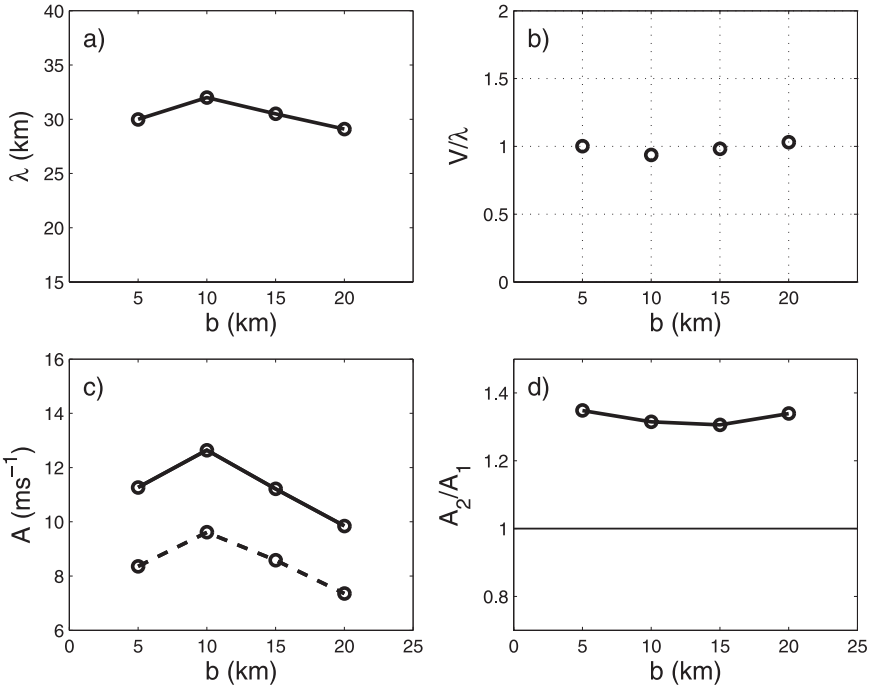

FIG. 11. As in Fig. 7 but for sensitivity experiments for the upstream mountain asymmetry; $H_n = 1$ and $V = 30$ km.

has a modulating effect on wave amplitudes, which are systematically reduced when the inversion is removed. This systematic depression of wave amplitudes, however, leaves the amplitude ratio essentially unaltered over the examined range of H_n values (Fig. 12d).

To further explore the effects of the inversion, we have conducted additional experiments without the inversion for $H_n = 1$ for a large subset of ridge separation distances (V) explored in section 4a(2). In these experiments, as in experiments with variable H_n, we found very little effect on the wavelength. Nevertheless, for certain valley widths, the lee-wave wavelength was found to alternate between the value in an equivalent experiment with the inversion and a longer value (e.g., for $V = 55$ km the primary wavelength alternates between 19.1 and 27.7 km during the quasi-steady period of the simulation; however, both of these nondimensional wavelengths are close to integer values). As before, the wave amplitudes are systematically lower than in the experiments with inversion, but the amplitude ratio in this case shows a radically different dependence on the ridge separation distance than in the presence of inversion, with no clear indication of interference patterns. Clearly, the inversion plays an important role in limiting the vertical propagation of wave energy and promoting reflection back toward the source region that, in turn, affects the interference of the excited lee waves.

2) VERTICAL WIND SHEAR

Here we separate the effects of vertical wind shear by keeping the constant stability profile from the previous section while altering the vertical wind shear in the troposphere. In these experiments $S \in [3,7]$ m s^{-1} km^{-1}, which includes 6.1 m s^{-1} km^{-1} for the baseline sounding (Table 1). The simulations were conducted for $H_n = 0$ and 1, $V = 30$ km, and $a = b = 5$ km. A limited number of experiments was also done for other values of V. As these simulations proved to be more sensitive to the position of lateral boundaries, the domain was enlarged to include 1001 points in the horizontal.

Vertical cross sections of potential temperature and vertical velocity for different values of S for $H_n = 1$ are shown in Fig. 13. Clearly, vertical wind shear exerts a more significant influence on lee waves than the inversion. Reducing wind shear results in a more regular and shorter-wavelength lee-wave train that extends farther downstream, likely due to reduced dissipation and turbulence in more laminar flows in these smaller-amplitude waves. The diagnostics summary in Fig. 14 shows a 60% reduction in wavelength for a reduction in shear by approximately 50% (from 6.1 m s^{-1} km^{-1} of the baseline sounding to 3 m s^{-1} km^{-1}). The nondimensional wavelengths cluster around integer values in this case, too, but V/λ increases as shear (S) decreases.

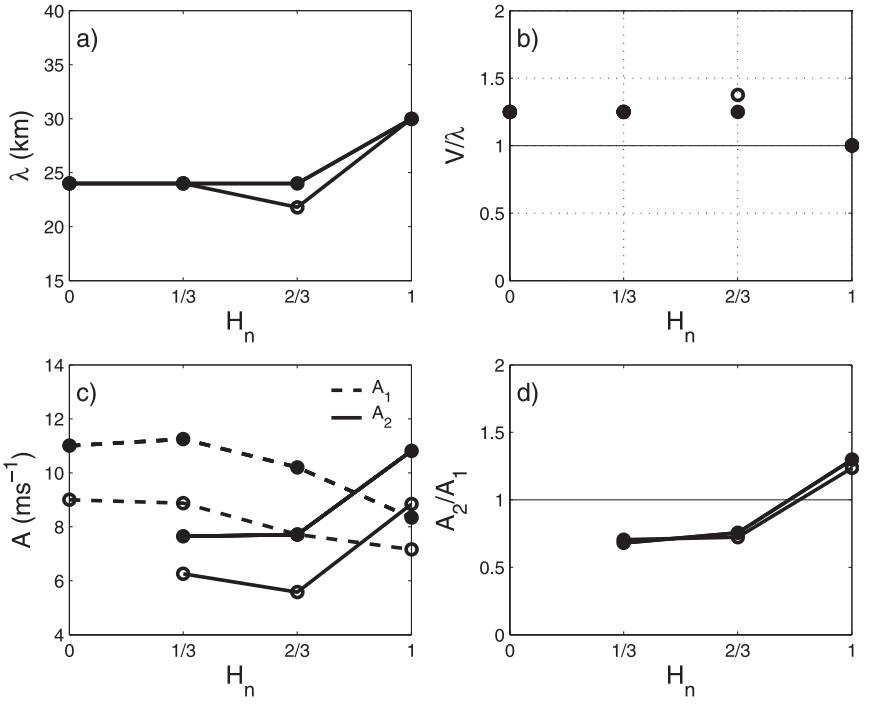

FIG. 12. As in Fig. 7 but for sensitivity experiments for the effects of inversion. Solid and open symbols denote experiments with and without the inversion; $H_n = 1$ and $V = 30$ km.

5. Discussion

In the preceding section we saw evidence of the twin peak separation distance exhibiting a strong control over the selection of lee-wave wavelengths and appearance of interferences. To explore these two points further, we have extended the range of terrain parameters covered in section 4a. A more systematic exploration through the parameter space, spanned by the mountain height ratio H_n and normalized ridge separation distance $V/2a$ (cf. Fig. 15), is summarized in Fig. 16, which shows wave drag, wavelengths, and amplitude ratios for three values of H_n (= 1/3, 2/3, 1) for a subset of ridge separation distances V examined in section 4a.

The results in Fig. 16 show that the two mountains that are close or equal in height ($H_n = 2/3$ and 1) produce an overall similar range of horizontal wavelengths and drag values. On the other hand, a downstream mountain of relatively small height ($H_n = 1/3$) excites longer waves that produce higher drag. Somewhat surprising, a small downstream mountain also exhibits a nonvanishing effect on the wave solution at large ridge separation distances, in spite of the amplitude ratio that decreases sharply toward zero as V is increased (Fig. 16b).

The fact that for any given V the wavelengths in Fig. 16 are different for the three H_n is an indication of the nonlinear nature of these waves since the corresponding orographic spectra have peaks, although of different amplitudes for different H_n, at essentially the same wavelengths.[2] This finding is not surprising given an inherent nonlinearity of the governing equations for lee waves, which makes nonlinear effects important even for relatively low mountains (Smith 1976; Nance and Durran 1998). One consequence of this is noninteger values of nondimensional wavelengths for $H_n \neq 1$.

The close match between the primary wavelength of the excited lee waves over twin peaks with the primary orographic wavelength of ~30 km for $H_n = 1$ and $V/2a = 3$, while intuitively expected, is really an exception. All other lee-wave wavelengths are shorter than the corresponding primary wavelength of the terrain, which is approximately equal to V for all valley widths (Fig. 17a). The nature of the relationship between the excited lee-wave wavelengths and the terrain forcing for $H_n = 1$ is more closely examined in Fig. 17. Whereas neither the primary wavelengths of the lee waves and the orography

[2] Differences in wavelengths associated with the individual peaks of the orographic spectra exist but are small. For example, the difference in the primary wavelength between $H_n = 1/3$ (34.78 km) and $H_n = 1$ (33.33 km) for $V = 30$ km is ~4%. Differences in higher harmonics of the primary wavelength are even smaller.

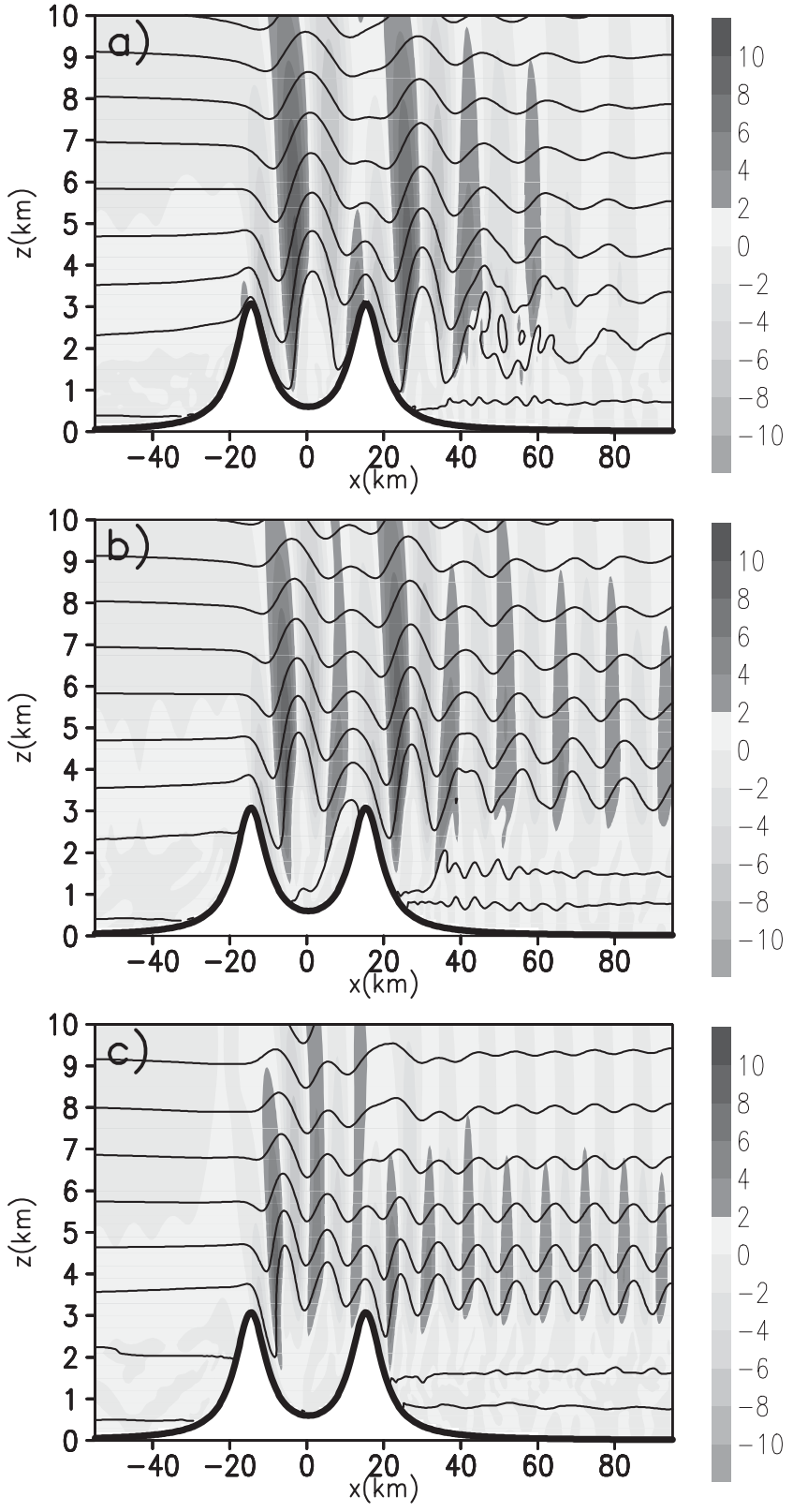

FIG. 13. As in Fig. 5 but for vertical wind shear (S) equal to (a) 5, (b) 4, and (c) 3 m s^{-1} km^{-1}; $H_n = 1$ and $V = 30$ km.

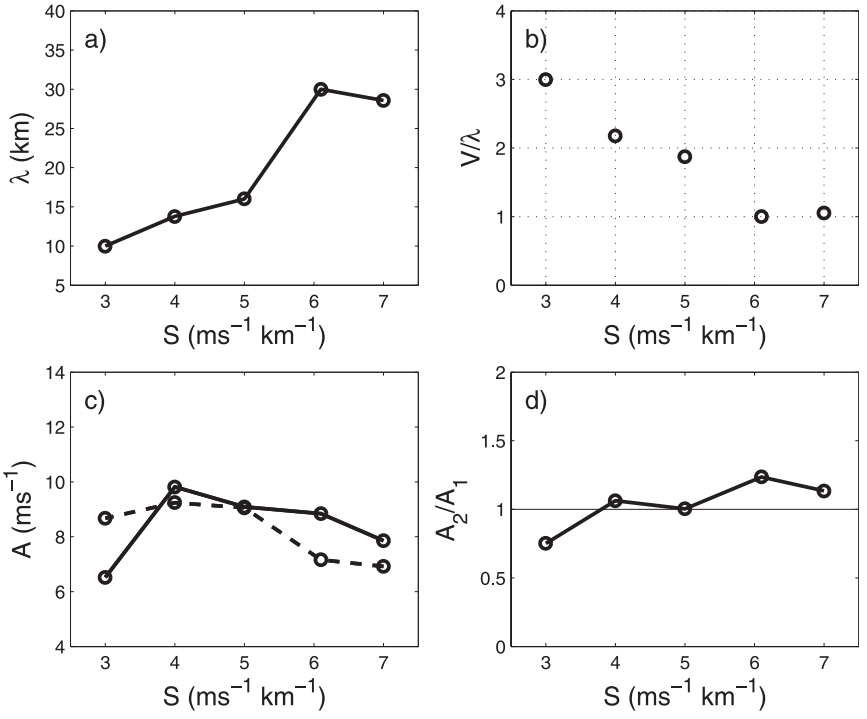

FIG. 14. As in Fig. 7 but for sensitivity experiments for vertical wind shear (S); $H_n = 1$ and $V = 30$ km.

nor the two higher harmonics, which carry most of the energy, appear to be well correlated (Figs. 17a–c), Fig. 17d shows that for any given V the primary lee-wave wavelength (λ) corresponds closely to one of the peaks of the respective orographic spectrum (cf. Fig. 4), up to the fifth harmonic of the primary orographic wavelength (λ_{oro}). This clearly shows that there is a preference in the system toward excitation of shorter horizontal wavelengths, those that are close to λ_s.

Points in the parameter space spanned by H_n and $V/2a$ for which positive and negative interferences have been detected are marked in Fig. 15. In determining whether a negative (destructive) or positive (constructive) interference, or resonance, has occurred for $H_n = 2/3$ and 1, we have identified minima and maxima in D (cf. Fig. 16a) as in Vosper (1996). The oscillations in D, although periodic (or quasi-periodic) with respect to V, are not identical for these two H_n (Fig. 16a), showing that resonance of these waves depends not just on the ridge separation distance but also on the ratio of mountain heights (cf. Durran 1986). The oscillation in values of D is mirrored in the oscillations of A_2/A_1 and λ in such as a way that negative interferences coincide with shorter wavelengths and smaller-amplitude ratios, whereas positive interference patterns are accompanied by longer wavelengths and larger-amplitude ratios.

Invoking a simple ''linear model'' of resonance (cf. Scorer 1997), one would expect positive interference for $V/\lambda_s \approx n$, where $n = 2, 3, \ldots$, for which the crest of the lee wave of wavelength λ_s coincides with the downstream peak, necessitating little or no adjustment to the lee-wave wavelength while producing a strong positive effect on amplitude. Alternately, for $V/\lambda_s \approx (2n - 1)/2$, where $n = 2, 3, \ldots$ negative interference would ensue due to a trough of the wave of wavelength λ_s falling on top of the downstream peak, producing a detrimental effect on the wave amplitude downstream.

Whereas in our experimental results there is limited evidence for the former, there is no evidence at all for the latter. Instead, for negative interference, the lee-wave wavelengths seem to undergo an adjustment to the closest shorter horizontal wavelength that is equal to an integer fraction of V, so that the nondimensional wavelength retains an integer value ($V/\lambda \approx n$). Thus (by equating the above two expressions), $\lambda = [1 - (2n)^{-1}]\lambda_s$ is obtained for negative interference, whereas $\lambda = \lambda_s$ for positive interference. As shown in Fig. 9a, this simple model explains the zigzag variation of the lee wavelength fairly accurately up to $V = 70$ km for $H_n = 1$. Even for $H_n = 2/3$, the mountain height ratio of Owens Valley, this model captures the observed variations for ridge separation distances $V < 45$ km. Clearly,

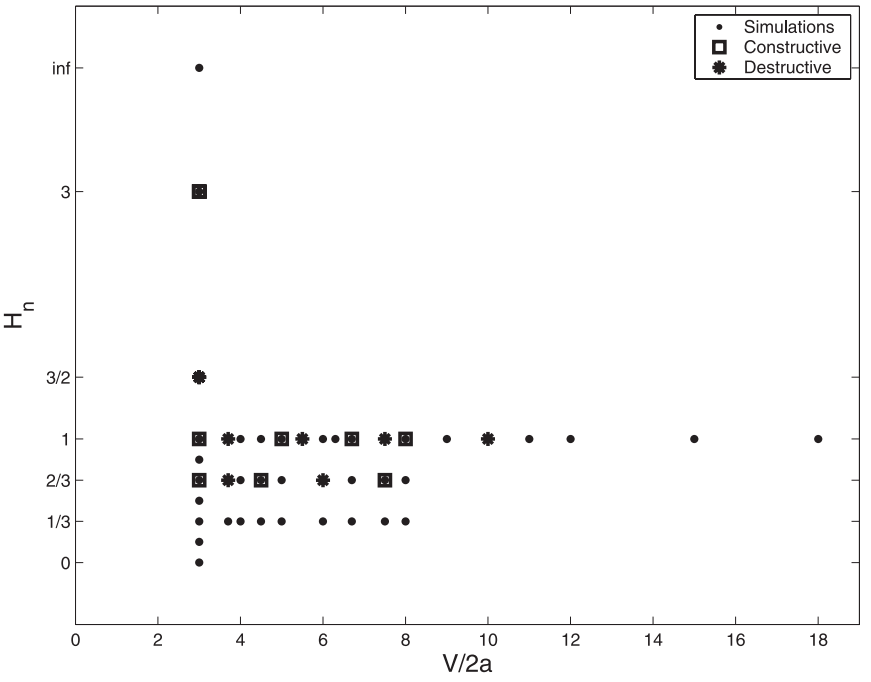

FIG. 15. Parameter space of the mountain height and valley width sensitivity experiments spanned by H_n and $V/2a$. Dots mark individual experiments. Runs for which constructive (square) and destructive interference (star) were detected are also marked.

at larger ridge separation distances other processes come into play for both of these H_n.[3] Also in our experiments, the wavelength adjustment appears to occur for both constructive and destructive interference. A good example of the constructive interference adjustment is the wave lengthening for $V = 30$ km.

The two interference patterns produce a significantly different flow over the downstream peak. For destructive interference, the flow over the downstream peak is symmetric, leading to a significant reduction in A_2 and the total drag (cf. Fig. 8a), whereas, under constructive interference, the wave solutions are characterized by a stronger flow asymmetry, larger lee-side amplitudes, and resulting high drag states.

To explain the above noted preference to wavelengths close to the intrinsic wavelength (λ_s), we have sought linear analytic models for which the Scorer parameter profile matches closely that of the baseline sounding (Fig. 2c) as linear steady-state lee-wave theory is known to predict wavelengths of trapped lee waves fairly accurately (while underpredicting their amplitudes; Smith 1976; Vosper 2004). The simplest one-layer approximations applicable to the l profile for the idealized upstream sounding are $l^2(z) \sim 1/S^2z^2$ (Wurtele 1953; cf. Queney et al. 1960), which correctly represents the influence of vertical wind shear, and $l^2(z) = l_0^2/\cosh^2[a(z\text{-}z_0)]$ (Tutiš 1992), which captures the effect of the inversion. The comparison between these two analytical functions and the baseline Scorer profile are shown in Fig. 18. The horizontal lee-wave wavelengths computed using linear model predictions are equal to $\lambda_T = 41$ km for the Scorer profile in Tutiš (1992) with $a = 110\ \text{m}^{-1}$, and $\lambda_W = 25$ km for $S = 6\ \text{m s}^{-1}\ \text{km}^{-1}$ for the linear shear profile in Wurtele (1953). The close match between the intrinsic wavelength ($\lambda_s = 24$ km) and the linear prediction including linear shear only ($\lambda_W = 25$ km) emphasizes the overall importance of wind shear as a primary trapping mechanism, consistent with the results from section 4b.

Predictions of the linear shear model of Wurtele (1953) also agree well with the variation of lee-wave wavelengths obtained for the range of linear shears (S) examined in section 4b(2) (Fig. 19a). Both the single peak ($H_n = 0$) and twin peak ($H_n = 1$, $V/2a = 3$) results shown in Fig. 19a show a similar variation of lee-wave wavelengths with shear, displaying an increase of lee-wave wavelengths as the strength of the shear is increased. For the twin peak orography, as shown in Fig. 19b, the lee-wave wavelengths are further modulated by the orographic spectrum. The result is a wave spectrum

[3] For $H_n \neq 1$, destructive interference patterns take different forms as illustrated in Fig. 5c and Fig. 6c for $H_n = 1/2$ and $H_n = 3/2$, respectively.

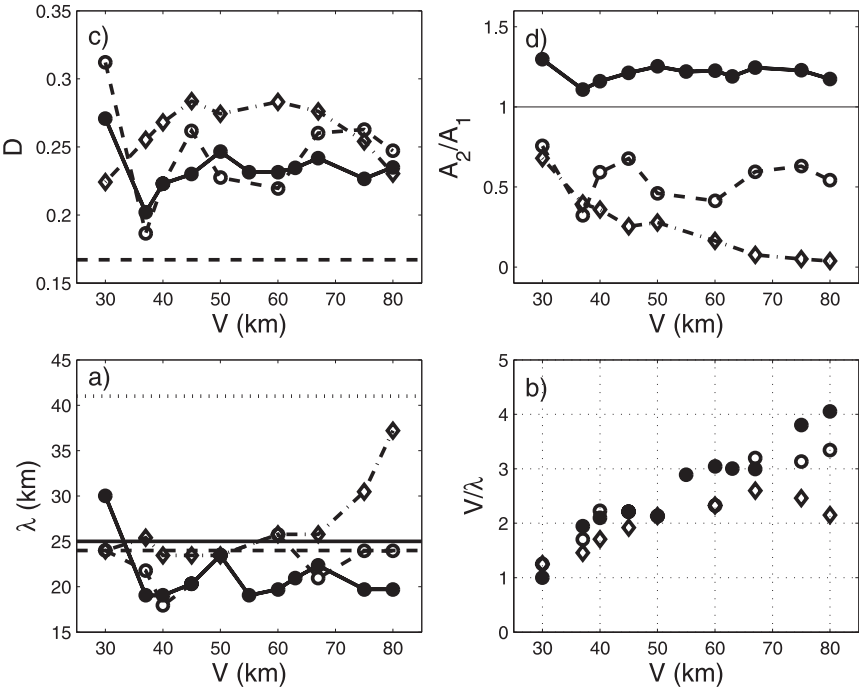

FIG. 16. Wave drag, wavelengths, and amplitudes for the mountain height and valley width sensitivity experiments as functions of V and H_n: (a) normalized drag (D), (b) amplitude ratio (A_2/A_1), (c) lee-wave wavelength (λ), and (d) nondimensional wavelength (V/λ), where $H_n = 1/3$ (dash-dotted line; diamonds), $H_n = 2/3$ (dashed line; circles), and $H_n = 1$ (solid line; stars). The horizontal lines in (c) indicate two linear theory predictions for lee-wave wavelengths for a single bell-shaped mountain [λ_W (Wurtele 1953), solid line, and λ_T (Tutiš 1992), dotted line] and the model prediction for $H_n = 0$ (long dashed line). The dashed line in (a) indicates drag value for $H_n = 0$.

that while dictated by the atmospheric vertical structure—primarily the vertical wind shear—is fine-tuned by the orographic spectrum in such a way that an integral multiple of lee-wave wavelengths corresponds to a given ridge separation distance. As shown in Fig. 17, this results in a shift toward shorter wavelengths in the spectrum of excited waves.

As the majority of experiments in this study were done with relatively narrow obstacles, the question remains as to what degree our findings are sensitive to the half-width of bell-shaped obstacles. Toward this end several additional experiments with broader mountains ($a = 10$ km and 15 km) for $V = 60$, 80, and 90 km were performed.[4] The results of these experiments are illustrated in Figs. 20 and 21 . Whereas the primary lee-wave horizontal wavelengths for $a = 5$ km and $a = 10$ km cluster around 20 km, for broader obstacles ($a = 15$ km) the primary horizontal wavelengths are longer and closer to 60 km (Fig. 20a). Longer lee-wave wavelengths for $a = 15$ km are consistent with a stronger forcing of hydrostatic waves by these broader obstacles. Nevertheless, as shown in Fig. 21, shorter trapped lee waves with horizontal wavelengths between 20 and 30 km are strongly excited for $a = 15$ km as well, as higher (secondary to quaternary) harmonics of a long wave that carries more energy. These shorter waves make a significant contribution to the total wave field. Whereas the scaling of primary lee-wave wavelengths with mountain half-width is not universal (Fig. 20c), all excited lee-wave wavelengths, including the primary one and the higher harmonics, remain close to integer fractions of the ridge separation distance (Fig. 20b). Thus, it appears that the ridge separation distance indeed plays a more important role in determining the horizontal trapped lee-wave wavelength than the mountain half-width, contrary to conclusions presented in Lee et al. (1987).

Despite our simulations being free-slip and no boundary layer separation being possible, in many of our experiments flow reversals underneath the first few wave crests are present. Clearly, baroclinic vorticity generation in these large-amplitude waves is strong enough to

[4] Only large values of V were chosen for these experiments to minimize the effects of increasing effective mountain heights and valley floors at large values of a.

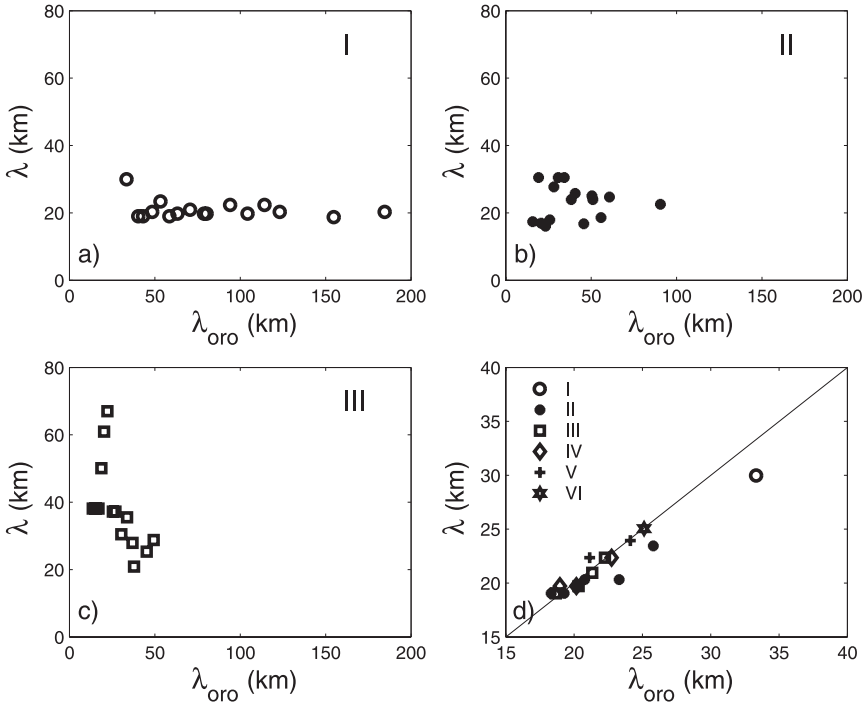

FIG. 17. Correlations between wavelengths of the primary spectral peak and two higher harmonics for lee waves (λ) and the terrain (λ_{oro}) for $H_n = 1$: (a) primary (I, circle), (b) secondary (II, star), and (c) tertiary (III, square) wavelengths. The relationship between the primary lee-wave wavelength and the closest matching orographic harmonic is shown in (d).

lead to the appearance of flow reversals and rotors in the absence of friction (cf. Doyle and Durran 2002). Unlike the lee-wave rotors produced under free-slip conditions by Doyle and Durran (2002), which were nonstationary and tended to propagate upstream, our lee waves and rotors are quite stationary. For mountain heights of 3 km, these flow reversals attain their maxima near 2 km above ground level and are strongest underneath the first wave crest in the immediate lee of an obstacle. These free-slip rotors are particularly strong for $H_n = 0$ (single mountain) and downwind of the downstream peak for $H_n = 1$ (twin peaks) under positive interference. Strong wind shear between the free streamflow in the wave and the flow reversal leads to the production of turbulent kinetic energy (TKE) and dissipation that causes attenuation of successive lee-wave amplitudes. Another likely cause of significant downwind decay of lee waves in our experiments is wave absorption (i.e., suppressed reflection) in the quiescent layer near the lower boundary, which owes its origin to the zero mean wind at the ground. As illustrated in Fig. 22, a simulation identical to the one illustrated in Fig. 5a—except for the mean wind profile with zero wind at the ground replaced by a 5 m s^{-1} wind at the ground while retaining the same vertical wind shear—produces significantly weaker lee-wave attenuation, consistent with findings of Smith et al. (2006).

6. Conclusions

In this idealized numerical study we investigated lee-wave patterns generated by double bell-shaped obstacles and explored their sensitivity with respect to the details of the terrain forcing and the vertical atmospheric structure. The terrain and the specific upstream atmospheric profile used in this study derive from the Sierra Nevada–Inyo Mountains and typical upstream atmospheric profiles observed during lee-wave events in Owens Valley in the Sierra Rotors Project and the Terrain-Induced Rotor Experiment.

The solutions, consisting of partially trapped lee waves, were found to exhibit strong sensitivity to the height of the secondary obstacle, whose presence was found to promote wave trapping and modulate wave amplitudes. For twin-peak mountains, and more generally for mountains that are relatively close in height, the ridge separation distance was found to exhibit a strong control over the selection of lee-wave horizontal wavelengths from a range of possible wavelengths supported by the given vertical atmospheric structure, primarily the

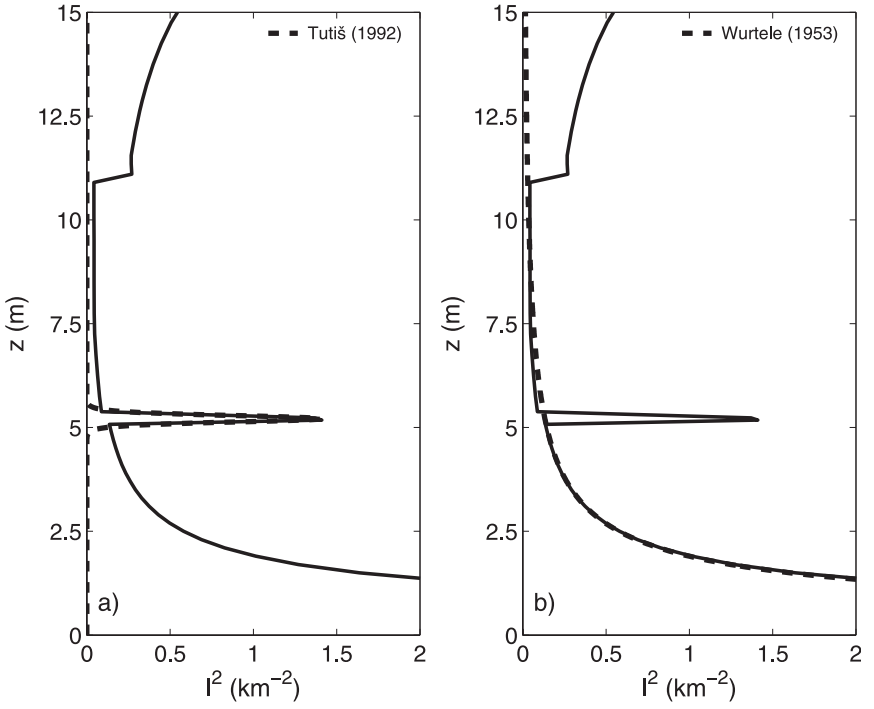

FIG. 18. Comparison of the Scorer parameter profiles for the baseline sounding (solid) and two analytical models (dashed): (a) Tutiš (1992) for $a = 110\ \mathrm{m}^{-1}$ and (b) Wurtele (1953) for $S = 6\ \mathrm{m\ s}^{-1}\ \mathrm{km}^{-1}$.

vertical shear of the horizontal wind. Wavelengths of lee waves excited by twin peaks were found to be equal to or shorter than waves excited by a single mountain; in addition, for twin peak orography, the primary lee-wave wavelengths were found to correspond to higher harmonics of the primary orographic wavelengths, with the latter approximately equal to the ridge separation distance. The result is a wave spectrum that, while dictated by the atmospheric vertical structure, is fine-tuned by the orographic spectrum in such a way that an integral multiple of lee-wave wavelengths corresponds to a given ridge separation distance.

The above was found to be true for both cases of positive and negative interference, which differ appreciably only in the flow structure over the downstream peak, with resulting differences in wave amplitudes and wave drag. The appearance of constructive and destructive interference for mountains that are close or equal in height was found to depend on both the ridge separation distance and the ratio of mountain heights.

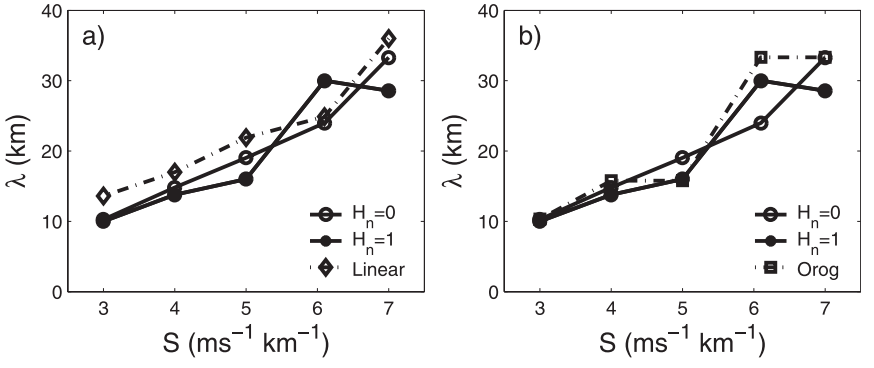

FIG. 19. Horizontal wavelengths as functions of linear shear strength S: (a) linear theory (Wurtele 1953) predictions and simulated values for $H_n = 0, 1$; (b) as in (a) except matching orographic wavelengths are shown in lieu of linear theory predictions.

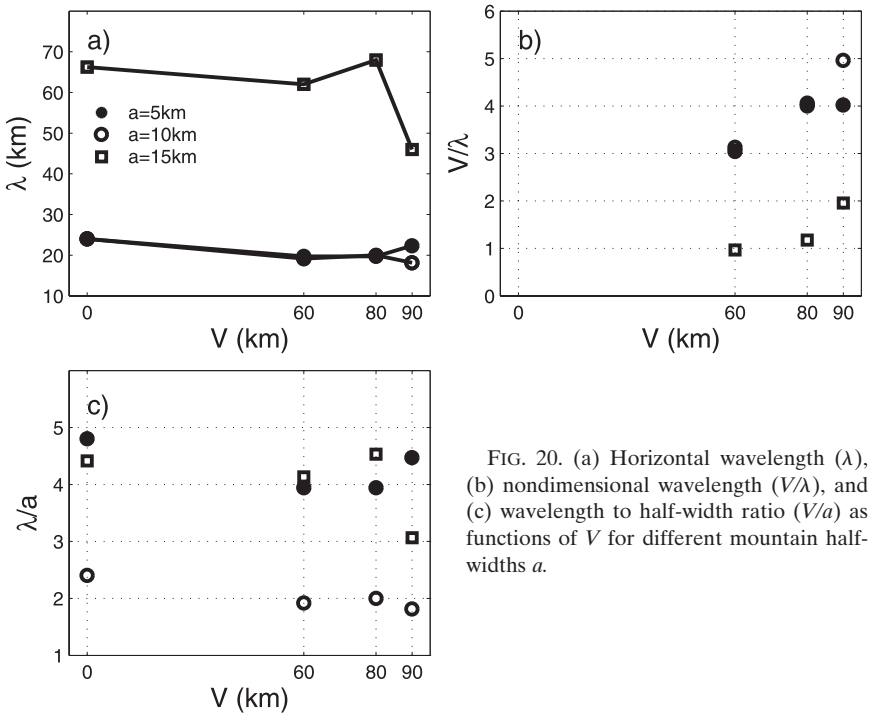

FIG. 20. (a) Horizontal wavelength (λ), (b) nondimensional wavelength (V/λ), and (c) wavelength to half-width ratio (V/a) as functions of V for different mountain half-widths a.

A simple ''linear resonance model with wavelength adjustment'' was found to describe resonant wavelengths fairly well for ridge separation distances of less than 45–60 km. Despite shear strongly controlling the horizontal wavelengths, the inversion was found to play an important role in determining the interference patterns.

The influence the two mountains exert on the overall lee-wave field was found to persist at large ridge separation distances, decaying much slower than for hydrostatic waves, even for fairly small downstream mountains. For these strongly nonlinear nonhydrostatic waves, the ridge separation distance was found to exert a much stronger control over the lee-wave wavelength than the mountain half-width.

For the mountain height ratio and valley width that correspond to Owens Valley ($H_n = 2/3$, $V = 30$ km), our idealized simulations produce lee waves with the horizontal wavelength that is equal to the ridge separation distance. Thus, there is only a single wave crest over the valley. In agreement with the sensitivity observed in the real case simulations of Grubišić and Billings (2007), two ridges in this case generate trapped lee waves with a wavelength that is about 20% longer than for waves generated by a single ridge. The amplitude of these waves is also larger over the valley than downwind of the downstream peak, in agreement with observations of waves in the T-REX IOP 6 event (Grubišić et al. 2008).

While our simulations are free-slip, regions of recirculating flow underneath lee-wave crests still form. The source of horizontal vorticity in these nonfrictional rotors is baroclinic generation in large-amplitude waves. In this context, we mention another role of the upstream inversion, which when placed at appreciable height above the mountain as was done in this study, enhances the lee-wave amplitude, and therefore promotes conditions favorable for rotor development. The flow stagnation within the valley also forms in our simulations despite the absence of the frictional boundary layer, likely owing its origin to the zero mean wind at the ground. In the presence of the frictional boundary layer, an additional set of flow realizations within valleys becomes possible, some of them due to wave-induced separation, as exemplified in studies by Bell and Thompson (1980), Tampieri and Hunt (1985), and Kimura and Manins (1988). The effects of frictional boundary layer on lee-wave resonances over double bell-shaped obstacle will be considered in our future studies.

Acknowledgments. This research was motivated by observations collected in the Sierra Rotors Project and the Terrain-Induced Rotor Experiment (T-REX), for which the primary sponsor was the National Science Foundation (NSF). The first author acknowledges support of NSF through Grant ATM–0524891 to DRI, and of NCAR through the Advanced Study Faculty Fellowship. The second author was supported by the

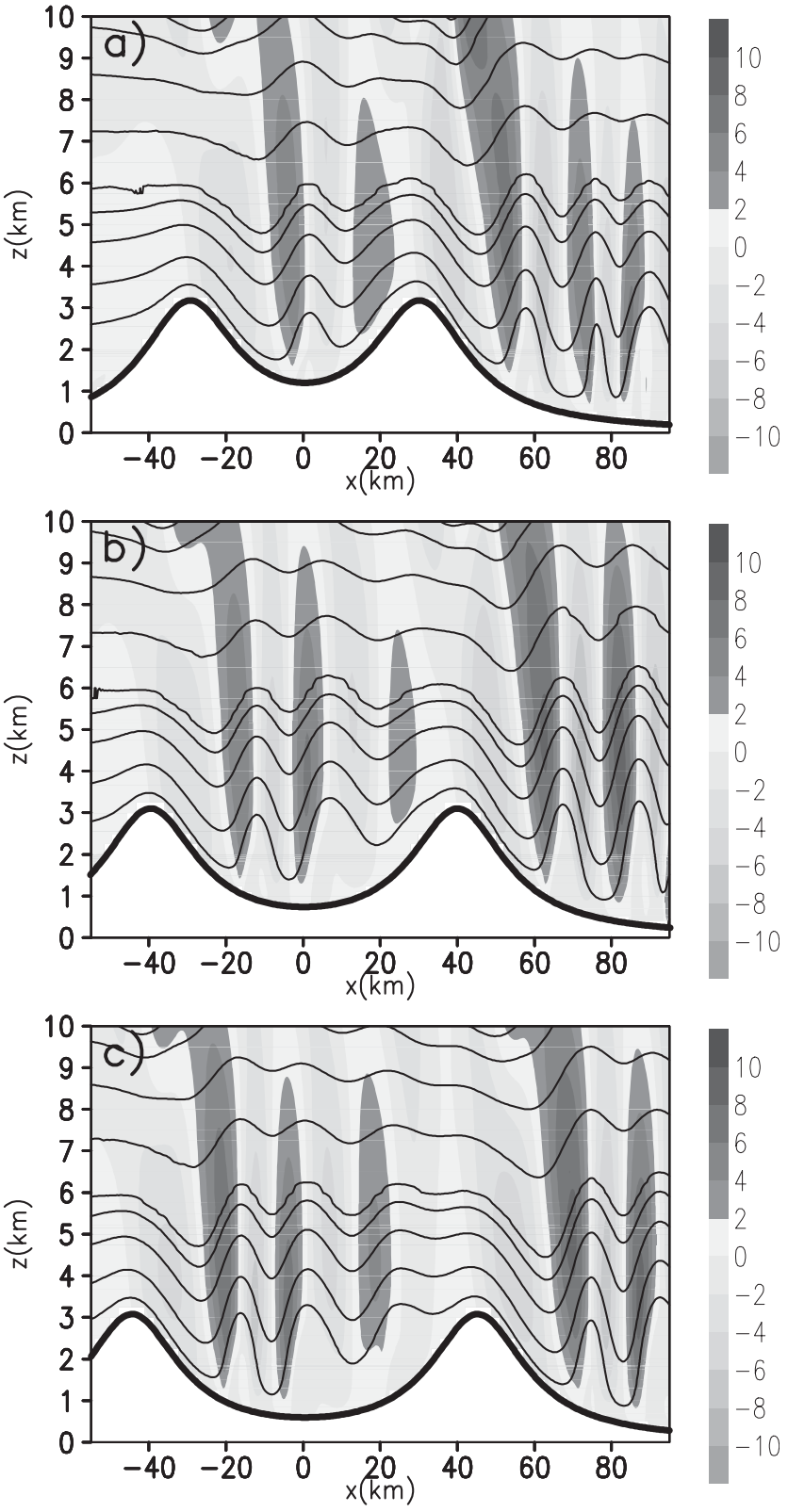

FIG. 21. As in Fig. 5 but for $H_n = 1$, a = 15 km, and valley width (V) equal to (a) 60, (b) 80, and (c) 90 km.

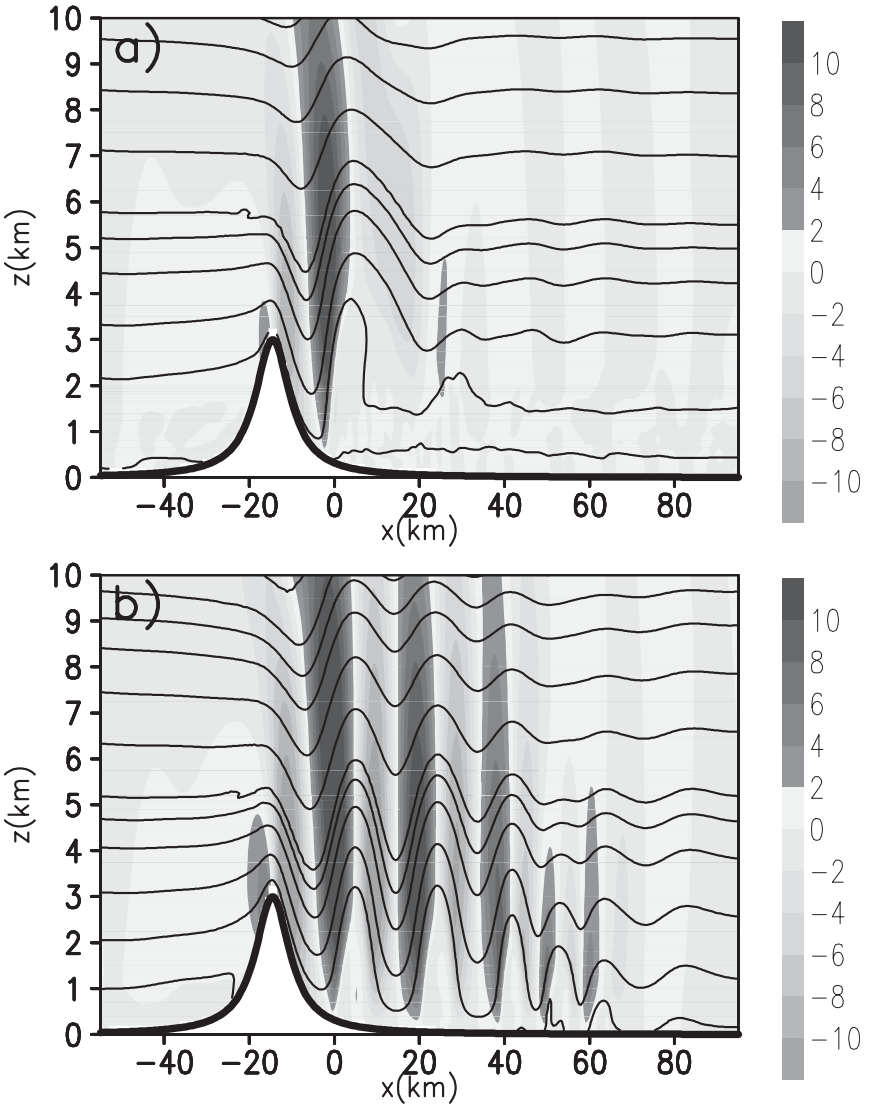

FIG. 22. As in Fig. 5 but for $H_n = 0$ at t = 12 h. The mean wind profile with zero wind at the ground in (a) is replaced in (b) by the 5 m s^{-1} wind at the ground while retaining the same vertical shear.

Croatian Ministry of Science through Grant 004-1193086-3036 to the Croatian Meteorological and Hydrological Service.

REFERENECS

Baines, P. G., 1995: *Topographic Effects in Stratified Flows*. Cambridge University Press, 482 pp.

Bell, R. C., and R. O. R. Y. Thompson, 1980: Valley ventilation by cross winds. *J. Fluid Mech.,* **96,** 757–767.

Doyle, J. D., and D. R. Durran, 2002: The dynamics of mountain-wave-induced rotors. *J. Atmos. Sci.,* **59,** 186–201.

——, V. Grubišić, W. O. J. Brown, S. F. J. De Wekker, A. Dörnbrack, Q. Jiang, S. D. Mayor, and M. Weissmann, 2009: Observations and numerical simulations of subrotor vortices during T-REX. *J. Atmos. Sci.,* **66,** 1229–1249.

Durran, D. R., 1986: Another look at downslope windstorms. Part I: The development of analogs to supercritical flow in an infinitely deep, continuously stratified fluid. *J. Atmos. Sci.,* **43,** 2527–2543.

Grisogono, B., S. C. Pryor, and R. E. Keislar, 1993: Mountain wave drag over double bell-shaped orography. *Quart. J. Roy. Meteor. Soc.,* **119,** 199–206.

Grubišić, V., and J. M. Lewis, 2004: Sierra Wave Project revisited: 50 years later. *Bull. Amer. Meteor. Soc.,* **85,** 1127–1142.

——, and B. Billings, 2007: The intense lee-wave rotor event of Sierra Rotors IOP 8. *J. Atmos. Sci.,* **64,** 4178–4201.

——, and Coauthors, 2008: The Terrain-Induced Rotor Experiment: A field campaign overview including observational highlights. *Bull. Amer. Meteor. Soc.,* **89,** 1513–1533.

Gyüre, B., and I. M. Jánosi, 2003: Stratified flow over asymmetric and double bell-shaped obstacles. *Dyn. Atmos. Oceans,* **37,** 155–170.

Hertenstein, R. F., and J. P. Kuettner, 2003: Rotor types associated with steep lee topography: Influence of the wind profile. *Tellus,* **57,** 117–135.

Hodur, R. M., 1997: The Naval Research Laboratory's Coupled Ocean/Atmosphere Mesoscale Prediction System (COAMPS). *Mon. Wea. Rev.,* **125,** 1414–1430.

Holmboe, J., and H. Klieforth, 1957: Investigations of mountain lee waves and the air flow over the Sierra Nevada. Department of Meteorology Final Rep., Contract AF 19(604)-728, UCLA, 283 pp.

Kimura, F., and P. Manins, 1988: Blocking in periodic valleys. *Bound.-Layer Meteor.,* **44,** 137–169.

Lee, J. T., R. E. Lawson, and G. L. Marsh, 1987: Flow visualization experiments on stably stratified flow over ridges and valleys. *Meteor. Atmos. Phys.,* **37,** 183–194.

Lee, Y., D. J. Muraki, and D. E. Alexander, 2005: A resonant instability of steady mountain waves. *J. Fluid Mech.,* **568,** 303–327.

Lilly, D. K., and J. B. Klemp, 1979: The effects of terrain shape on nonlinear hydrostatic mountain waves. *J. Fluid Mech.,* **95,** 241–261.

Lozovatsky, I. D., E. G. Morozov, and H. J. S. Fernando, 2003: Spatial decay of energy density of tidal internal waves. *J. Geophys. Res.,* **108,** 3201, doi:10.1029/2001JC001169.

Mayr, G. J., and A. Gohm, 2000: 2D airflow over a double bell-shaped mountain. *Meteor. Atmos. Phys.,* **72,** 13–27.

Mellor, G. L., and T. Yamada, 1982: Development of a turbulence closure model for geophysical fluid problems. *Rev. Geophys. Space Phys.,* **20,** 851–857.

Miller, P. P., and D. R. Durran, 1991: On the sensitivity of the downslope windstorms to the asymmetry of the mountain profile. *J. Atmos. Sci.,* **48,** 1457–1472.

Nance, L. B., and D. R. Durran, 1998: A modeling study of nonstationary trapped mountain lee waves. Part II: Nonlinearity. *J. Atmos. Sci.,* **55,** 1429–1445.

Pierrehumbert, R. T., and B. Wyman, 1985: Upstream effects of mesoscale mountains. *J. Atmos. Sci.,* **42,** 977–1003.

Queney, P., G. A. Corby, N. Garbier, H. Koschmieder, and J. Zierep, 1960: The airflow over mountains. WMO Tech. Note 34, 135 pp.

Reinecke, P. A., and D. R. Durran, 2009: The overamplification of gravity waves in numerical solutions to flow over topography. *Mon. Wea. Rev.,* in press.

Scorer, R. S., 1949: Theory of waves in the lee of mountains. *Quart. J. Roy. Meteor. Soc.,* **75,** 41–56.

——, 1997: *Dynamics of Meteorology and Climate*. Wiley, 686 pp.

Smith, R. B., 1976: The generation of lee waves by the Blue Ridge. *J. Atmos. Sci.,* **33,** 507–519.

——, 1979: The influence of mountains on the atmosphere. *Advances in Geophysics,* Vol. 21, Academic Press, 87–230.

——, Q. Jiang, and J. D. Doyle, 2006: A theory of gravity wave absorption by a boundary layer. *J. Atmos. Sci.,* **63,** 774–781.

Tampieri, F., and J. C. R. Hunt, 1985: Two-dimensional stratified flow over valleys: Linear theory and laboratory investigation. *Bound.-Layer Meteor.,* **32,** 257–279.

Tutiš, V., 1992: Trapped lee waves: A special analytical solution. *Meteor. Atmos. Phys.,* **50,** 189–195.

Vosper, S. B., 1996: Gravity-wave drag on two mountains. *Quart. J. Roy. Meteor. Soc.,* **122,** 993–999.

——, 2004: Inversion effects on mountain lee waves. *Quart. J. Roy. Meteor. Soc.,* **130,** 1723–1748.

Wang, T. A., and Y. L. Lin, 2000: Effects of shear and sharp gradients in static stability on two-dimensional flow over an isolated mountain ridge. *Meteor. Atmos. Phys.,* **75,** 137–164.

Wurtele, M. G., 1953: Studies of lee waves in atmospheric models with continuously distributed static stability. Science Rep. 4, Contract AF 19(122)-263, UCLA, 10 pp.

——, R. D. Sharman, and T. L. Keller, 1987: Analysis and simulations of a troposphere–stratosphere gravity wave model. Part I. *J. Atmos. Sci.,* **44,** 3269–3281.

——, ——, and A. Datta, 1996: Atmospheric lee waves. *Annu. Rev. Fluid Mech.,* **28,** 429–476.

——, A. Datta, and R. D. Sharman, 1999: Unsteadiness and periodicity in gravity waves and lee waves forced by a fixed rigid boundary. *J. Atmos. Sci.,* **56,** 2269–2276.